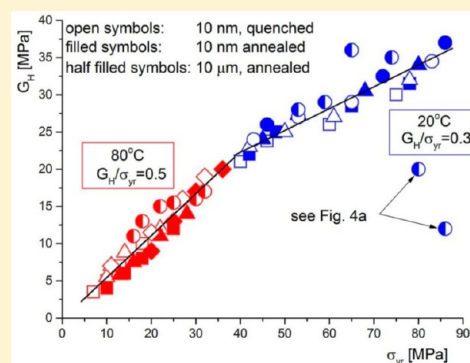


Effect of Particle Size, Temperature, and Deformation Rate on the Plastic Flow and Strain Hardening Response of PMMA Composites

Josef Jancar,^{*,†} Robert S. Hoy,[‡] Alan J. Lesser,[§] Ema Jancarova,[†] and Jan Zidek[†][†]CEITEC, Brno University of Technology, 61200 Brno, Czech Republic[‡]Department of Physics, University of South Florida, Tampa, Florida, 33620, United States[§]Department of Polymer Engineering and Science, University of Massachusetts, Amherst, Massachusetts, 01003, United States

ABSTRACT: We present extensive studies of the nonlinear mechanics of neat, microparticle (MP) and/or nanoparticle (NP) filled PMMA. Rigid particles are used as “probes” that alter local chain packing, the degree of correlated molecular motion, and structural relaxation times. We show that the extent of these alterations are proportional to the specific particle–PMMA interface area and the spatial distribution of interparticle distances. Nanoparticles are used to maximize these probe effects because both their size (D) and the distance between them (D_{NP}) are of order the radius of gyration of the polymer chains at low NP volume fractions. We analyze the effects of MPs and NPs on the elastic moduli and postyield response for samples prepared with different thermal histories and deformed at a range of temperatures and strain rates. In particular, we exploit qualitative differences between the response of PMMA composites deformed at $T_{lo} = T_g - 80$ K and $T_{hi} = T_g - 20$ K to illustrate key features of the relationship between the mechanically rejuvenated yield stress, σ_{yr} , and strain hardening modulus, G_H . The observed trends are supported by kinetic analyses and exploited to test recently proposed models of plastic flow and strain hardening. Our results should lead to an improved understanding of the factors controlling the ultimate performance of polymer composites.



INTRODUCTION

Since yield, strain softening, and strain hardening responses govern the extent of strain localization and the nature of failure processes that occur in glassy polymers,¹ understanding the structural variables that affect the large strain mechanical response is crucial for engineering polymeric and nanocomposite materials with tailorable mechanical properties. Our understanding of the physics controlling the nonlinear mechanics of glassy polymers has improved dramatically over the past several years,^{2–25} yet it remains far from complete. One major reason for this is that relaxation mechanisms critical to mechanical response are associated with a wide range of controlling energy, length and time (E , L , and T) scales that are often not well separated. Different relaxation mechanisms are dominant in different mechanical regimes (e.g., systems begin exploring their energy landscapes via the α - and β -processes near yielding, while relaxation of the entanglement mesh and chain scission control fracture),²⁶ and their competition/cooperation with one another depends on stress, strain, strain rate, temperature, and thermo-mechanical history.^{2–25} It is perhaps unsurprising, then, that despite their enormous technological importance, no theory has yet been developed that satisfactorily treats the entire range of glassy polymers' mechanical response.

Modern constitutive models now accurately describe yield, strain softening, and strain hardening at a phenomenological level.^{4–8} However, the underlying molecular models of large strain mechanical response in nonequilibrium polymer glasses

remain in a rapid state of development. Currently, the polymer nonlinear Langevin equation theory (PNLE) is probably the most complete microscopic theory for the nonlinear mechanical response and relaxation of polymer glasses.^{16–19} The PNLE theory predicts that beyond the yield point, large deformation induces anisotropic chain conformations resulting from modified chain packing, suppressed density fluctuations, enhanced dynamic constraints and retarded segmental relaxations. These effects are expressed in terms of relationships between the applied stress, external deformation, and the glassy physics encoded in an effective dynamical free energy F_{eff} that controls activated barrier hopping. It assumes applied stress (as encoded by the structure factor $S(q)$) alters segment-scale ordering. Varying the mechanically generated disorder alters the amplitude S_0 of local density fluctuations, thereby altering the segment-scale relaxation times and the slope of the stress–strain curve. This theory has been shown to capture a broad range of phenomena including strain softening, plastic flow, and strain hardening in both creep and constant-strain-rate deformation.

High-performance polymer materials are often made by adding purpose-specific NPs into a polymer matrix. Nanoscale fillers strongly affect the ordering and relaxation dynamics of the surrounding polymeric matrix, producing property changes such

Received: May 9, 2013

Revised: November 6, 2013

Published: November 26, 2013

as enhanced stiffness, strength and toughness that are valuable for engineering applications.²⁷ They have been shown in many studies to produce stronger effects than micrometer-size particles at the same loading (i.e., particle volume fraction). Our current theoretical understanding of glassy nanocomposite mechanics is even less complete than that for neat polymer glasses. Nonetheless, the very fact that nanoscale fillers affect ordering and relaxation dynamics—and with them mechanical response—allows them to be used as segmental-length-scale probes.

The aim of this paper is to obtain a better understanding of glassy-polymer and nanocomposite mechanics through systematic investigations of how the thermal and mechanical response varies with nanofiller and microfiller loading, thus allowing separation of particle excluded-volume and particle–PMMA interface related effects. Micrometer-sized fillers with small specific interface area do not disturb segmental mobility and packing in a significant volume of PMMA; their effects on the rejuvenated yield stress and strain hardening modulus can be described by a simple volume replacement model analogous to the Einstein–Batchelor law for the viscosity of suspensions ($\eta(\nu_f)/\eta(0) = 1 + 2.5\nu_f + K\nu_f^2$). Nanoparticles, however, modify the dynamics and packing on the segmental scale in PMMA. We demonstrate these effects by subjecting neat and composite PMMA to deformation at a variety of strain rates and temperatures, focusing on how rigid nano and micro particles (NPs, MPs) alter the plastic flow and initial strain hardening regimes. We show that the large specific surface area nanoparticles can be effectively used as probes that alter the local chain packing efficiency and dynamics, allowing us to test recently proposed models of mechanical response in these regimes. The use of a single matrix polymer, PMMA, both isolates chain-packing effects from other chemistry-dependent factors and allows for comparison to model predictions for neat PMMA.^{16–19}

The effects of NPs on the strain hardening response of PMMA depend weakly on thermal history, and very strongly on temperature and strain rate. In particular, we exploit qualitative differences between the response of systems deformed at $T_{lo} = T_g - 80$ K and $T_{hi} = T_g - 20$ K, and between systems deformed at low and high rates, to illustrate key features of the relationship between the flow stress (σ_{yr}) and strain hardening modulus (G_H). At T_{lo} , the NP volume fraction (ν_f) dependences of σ_y and G_H agree well with predictions from the above-mentioned volume-replacement model, while at T_{hi} , large deviations from this model indicate substantial alteration of segmental dynamics and packing at the NP-matrix interface. The scaling of G_H with σ_{yr} is linear (with a temperature-dependent slope¹³), consistent with models that predict flow and hardening are controlled by similar microscopic processes.^{10–12,17–19,30,31} With increasing ν_f , the linear G_H – σ_{yr} scaling is preserved, but exhibits a shift to larger G_H that we show is proportional to the specific PMMA–SiO₂ interface area, S_f . We explain these effects in terms of the good NP dispersion in our samples and detailed kinetic analyses of σ_{yr} and G_H . In particular, measured activation energies and volumes for both strain hardening and plastic flow are consistent with the above empirical observations. Our results should lead to an improved understanding of the various factors controlling the ultimate performance of polymer nanocomposites.

MATERIALS AND METHODS

Fumed silica nanoparticles (SiO₂, Sigma-Aldrich) with the specific surface area of 390 m²/g (BET, Quantachrome, USA) and primary particle diameter (TEM, Quanta, FEI CZ) of 10 nm (Figure 1a) and

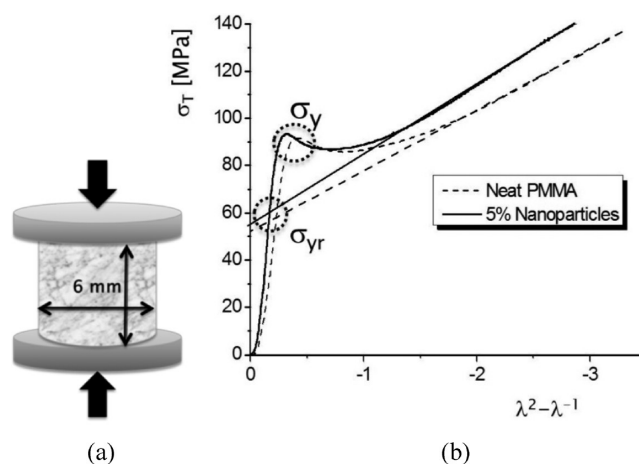


Figure 1. (a) Test geometry and (b) yield, σ_y , and mechanically rejuvenated yield, σ_{yr} , stress data acquisition scheme.

glass beads with average particle diameter (Zetasizer) of (10 ± 4) μm and specific surface area (BET) of 0.3 m²/g (Figure 2c) were used as the fillers. The sample preparation protocol was identical for all the composites investigated. The PMMA used (Plexiglas 8N, Evonik, Germany) has $M_n = 68$ kg mol⁻¹, $M_w/M_n = 1.7$ and $T_g = 376$ K (DMA, 1 Hz, 3 K/min.).

The filler was mixed with the PMMA in 1:1 acetone:toluene solvent using an ultrasound dispersion tip. After vigorous mixing for 3 h to obtain uniform NP and MP dispersion (Figure 2, parts b and d), the mixture was cast into a film and dried at 80 °C in a vacuum oven. The dried films were milled under liquid nitrogen and the powders were compression molded at 180 °C into cylindrical specimens with height and diameter equal to 6 mm (Figure 3). The neat PMMA underwent the same sample preparation procedure. Uniaxial compression experiments were performed at constant true strain rate employing a mechanical tensile and compression tester Instron 5800 (Instron, USA) using the cylindrical samples with surface to volume ratio of 1. All experiments were performed at constant true compressive strain rates ranging from 10^{-4} to 10^{-1} s⁻¹ and at temperatures ranging from $T_{lo} = T_g - 80$ K (20 °C) to $T_{hi} = T_g - 20$ K (80 °C). Temperature effects on true stress–strain curves due to internal heat generation, reported in the literature⁵ for samples with surface to volume ratios smaller than 1, were neglected in our work.

To prevent barreling of the sample due to friction, a thin film of Teflon tape (3 M 5480) was attached to the sample ends and the platens were lubricated with a silicon oil spray, dramatically reducing the friction between sample and platens. The sample dimension along the compression direction was calculated from the cross-head displacement of the tensile tester and corrected for the finite compliance of the entire test setup before data acquisition. The instantaneous lateral sample dimension of the cylindrically symmetric sample as a function of compressive strain was calculated assuming the PMMA is incompressible.⁶

Prior to measurements, specimens were either annealed at $T_{hi} = T_g - 20$ K for 10⁴ s, followed by cooling to room temperature at the cooling rate of 10⁻³ K s⁻¹ (referred to as “annealed”) or heated at $T = T_g + 20$ K for 4×10^3 s, followed by quenching to room temperature at the cooling rate of 4×10^{-1} K s⁻¹ (referred to as “quenched”). Thus, the annealed samples are also moderately aged, while quenched samples are not aged and show a closer-to-“intrinsic” response.³ Properties of the neat PMMA are shown in Table 1.

Specimens 5 mm \times 20 mm \times 0.5 mm for dynamic mechanical analysis (DMA) were cut from the compression molded sheet using a rectangular shaped steel cutter. DMA measurements were performed employing the AR G2 DMA (TA Instruments, USA) using torsion geometry. Temperature sweeps from 40 to 160 °C were performed at constant frequency 1 Hz and amplitude deformation of 0.01%. For all measurements, an average over three measurements was calculated; a standard deviation smaller than 8% was obtained.

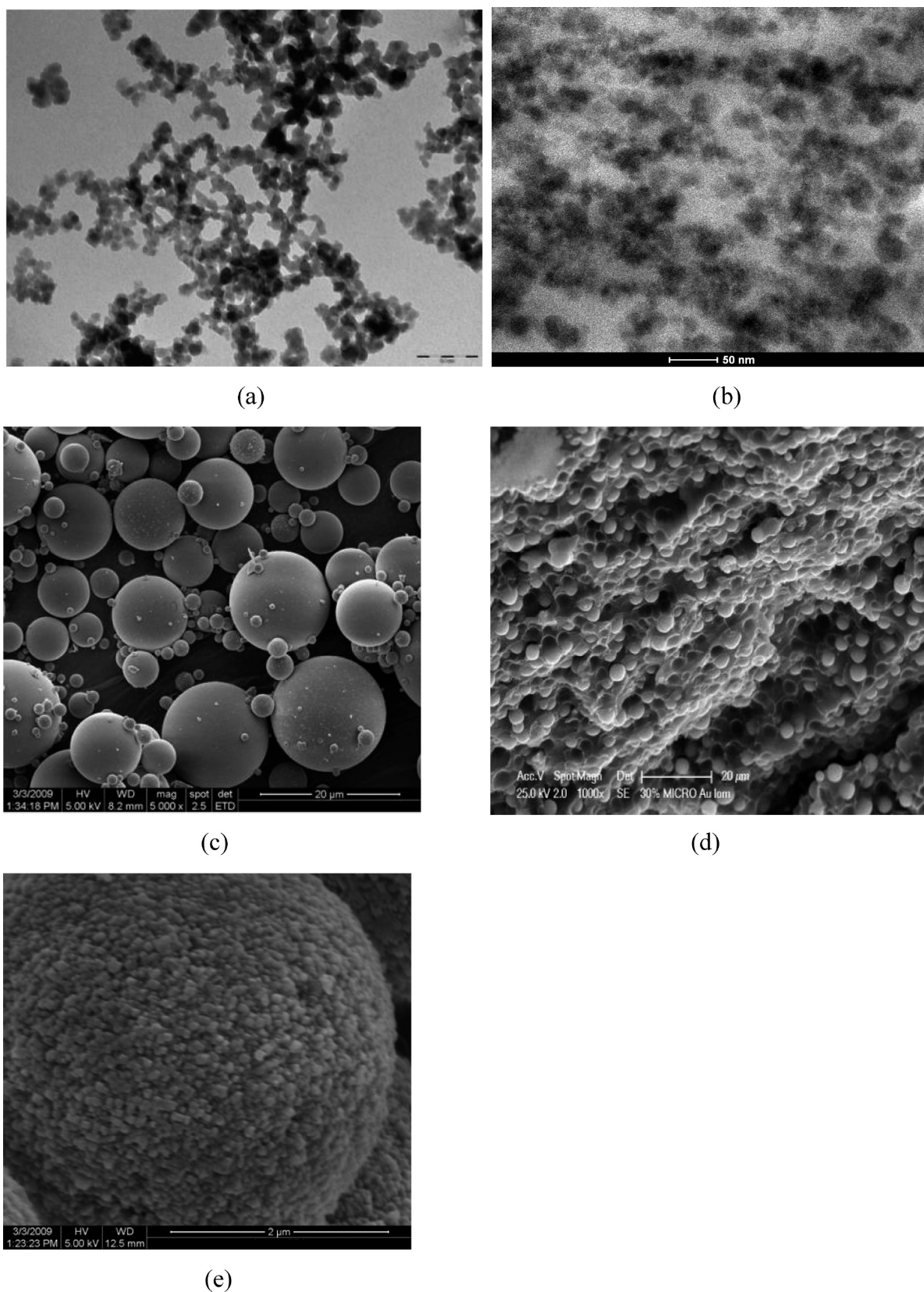


Figure 2. (a) TEM of the fumed silica used as the filler and (b) TEM of the PMMA containing 5 vol % of the silica shown in part a. The SiO₂ strings shown in part a consisted of primary particles with the diameter $D \approx 10$ nm. The scale bar in both micrographs represents 50 nm. (c) SEM of the glass beads used as the microfiller with average particle diameter (Zetasizer) of (10 ± 4) μm and specific surface area (BET) of $0.3 \text{ m}^2/\text{g}$. (d) SEM micrograph of the PMMA containing 30 vol % glass beads fractured in liquid nitrogen. The scale bar in both micrographs represents 20 μm . (e) SEM of the fused SiO₂ microfiller particle with average particle diameter (Zetasizer) of (5 ± 2) μm and specific surface area (BET) of $2.8 \text{ m}^2/\text{g}$.

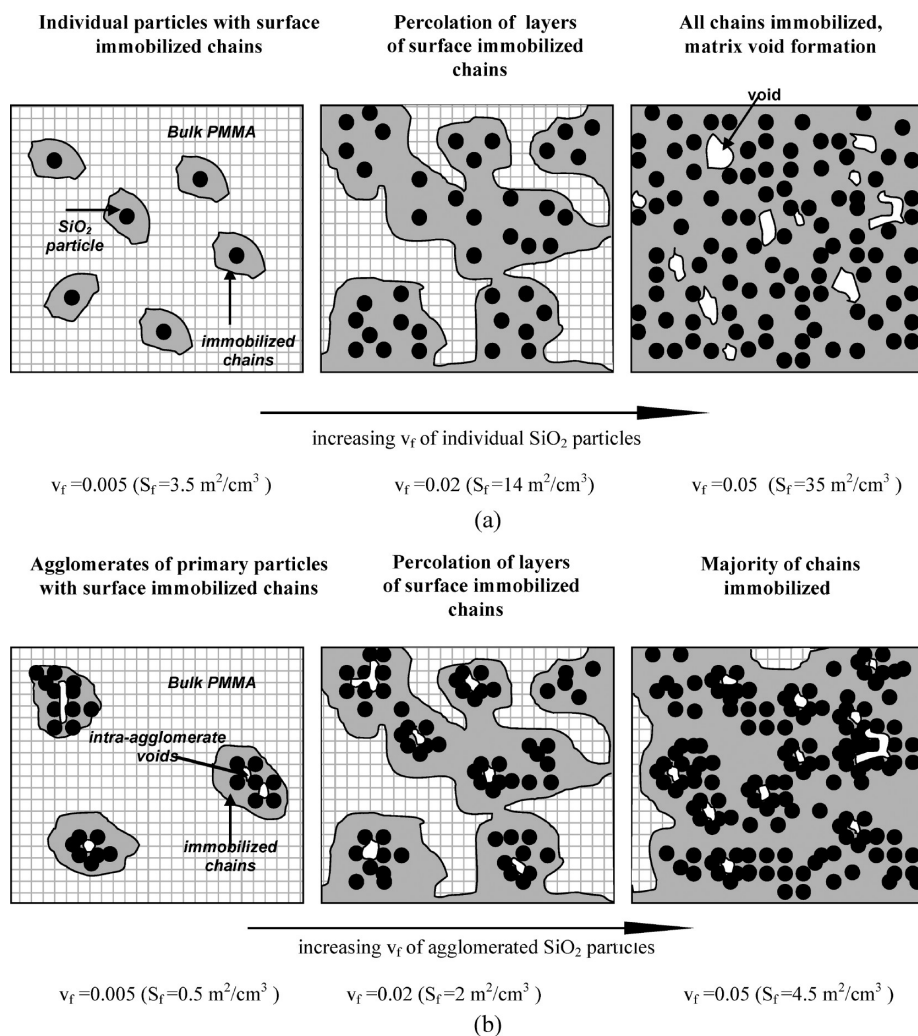


Figure 3. Simple 3-phase model of the structure of PMMA filled with individual SiO₂ NPs (a) and agglomerated NPs (b) as a function of filler volume fraction or specific interface area.

Table 1. Yield, σ_y , and Rejuvenated Yield, σ_{yr} , Strength of the Neat PMMA Measured at $T_{lo} = T_g - 80$ K and $T_{Hi} = T_g - 20$ K at the Compressive Strain Rate of 10^{-2} s^{-1} for the Two Thermal Histories Investigated

T [K]	annealed σ_y [MPa]	annealed σ_{yr} [MPa]	quenched σ_y [MPa]	quenched σ_{yr} [MPa]
$T_{lo} = 293$	107 ± 5	57 ± 5	87 ± 4	52 ± 6
$T_{Hi} = 353$	19 ± 2	11 ± 3	16 ± 1	9 ± 2

The strain hardening modulus, G_{Hj} , was determined from the slope of the true stress–Green–Lagrange strain curves following conventional experimental protocol for compressive straining by assuming constant-volume deformation in the strain interval from $1.75 < (\lambda^{-1} - \lambda^2) < 3.0$. Values of G_{Hj} were calculated from an average of five independent measurements for every composition and test condition (T , $d\epsilon/dt$, v_f); standard deviations among these measurements were less than 15%. The yield strength, σ_y , was determined as the first maximum on the true stress–true strain curve, and the rejuvenated yield stress, σ_{yr} , was the intercept of the stress–strain curve and the linear extension of the strain hardening region (Figure 1). Note that when strain softening and strain hardening regimes overlap, measurement of a “true” plastic flow stress is not straightforward¹⁹ since both hardening and softening are simultaneously operative. In particular, both the stress and strain at which the stress minima occur will be preparation-protocol-dependent. However, the quantity σ_{yr} should be only weakly dependent on

preparation protocol and can be identified with the steady-state plastic flow stress that would be present in the absence of strain hardening¹⁹ (Figure 1). Therefore, in the below, we analyze the scaling of PMMA mechanics with nanoparticle loading, temperature and strain rate in terms of the two quantities σ_{yr} and G_{Hj} .

RESULTS AND DISCUSSION

The dispersion of particles in glassy matrices is known to play a critical role in polymer composite mechanics.²⁸ Significantly different particle packing may be required to optimize different physical properties in these systems. Reducing particle size from micrometer to nanometer scale may amplify this problem substantially.²⁷ For example, well-dispersed NPs can act as “entanglement attractors”, thereby increasing toughness.³² Alternatively, in the case of attractive NP-NP interactions, the NPs can phase-separate from the matrix and form dense clusters with reduced “exposed” surface area and corresponding reductions in the extent of their thermomechanical influence. The fumed silica fillers employed here are known for forming string-like aggregates which may be up to 200 nm in length for 10 nm-diameter primary NPs. These strings may be quite flexible, behaving to a certain extent similarly to worm like chains. However, they are fragile and can easily break upon mixing.^{33–35}

We therefore begin by characterizing the state of NP dispersion in our systems. Figure 2 shows TEM images of the

fumed silica before addition to the PMMA, as well as silica dispersed within the PMMA after the mixing and cooling process described above. Before mixing, the silica spheres form strings which in turn form fractal-like aggregates (Figure 2a). Strings are apparently randomly arranged on top of each other in layers, forming a 3D percolating network system. After blending with PMMA, a far more homogeneous distribution of silica NPs is observed (Figure 2b) due to the disintegration of the NP strings in the process of mixing described above. The NPs do not form dense clusters, but tend to assemble into string-like aggregates wherein most NPs are exposed to polymer and the interfacial NP–polymer surface area is large. Despite the string-like structure of fumed silica used in this work, the BET measured SiO_2 specific surface area of $390 \text{ m}^2/\text{g}$ is still large and approximately equal to the theoretical value calculated for 1 g of monodisperse 10 nm NPs with density of $2.2 \text{ g}/\text{cm}^3$. Hence, it seems reasonable to assume that most of the silica surface area is available for interaction with polymer chains. For simplicity, we therefore hypothesize in the below discussion that NP dispersion in undeformed samples is characterized by random positioning of individual NPs within the polymer matrix. As described below, we envision and provide evidence below that the above-mentioned volume-replacement models for σ_{yr} and G_H fail at $T = T_{hi}$ (but not at $T = T_{lo}$) because of modified chain packing and retarded segmental dynamics in the vicinity of well-dispersed NPs.

Unlike fumed silica, the glass beads used as the micro filler (Figure 2c) do not form strongly bound aggregates or clusters and disperse in PMMA relatively uniformly (Figure 2d). Because of their small specific interface area, S_f , significantly greater filler loading can be achieved compared to large S_f silica nano filler.

Nanoparticles introduce a large specific interfacial surface into the polymer matrix, amplifying effects on segment-scale packing and relaxation mechanisms that are negligible in polymers filled with micrometer-sized particles. In particular, NP spatial packing is of great importance when particle diameter, D , is comparable to the polymer radius of gyration, R_g ;^{27,36,37} our NP-filled systems are in this regime. In order to obtain a reasonably simple description of the structure–property relationships, we assume three characteristic structures are present: (i) isolated individual NPs, (ii) multiple-NP clusters with interparticle distance on the order of R_g , and (iii) multi-NP agglomerates with interparticle distance shorter than R_g . These are illustrated in Figure 3.

To further elucidate the NP dispersion within the context of the three-phase model, we simulated NP dispersion by randomizing the distribution of the three limiting structures (Figure 3) and obtaining their relative population fractions as a function of v_f using a technique described in ref 38. As shown in Figure 4, at $v_f = 0.01$, for random spatial arrangement of monodisperse spherical particles, the shortest interparticle distance, l_p , is equal to the NP diameter, $D = 10 \text{ nm}$, which is

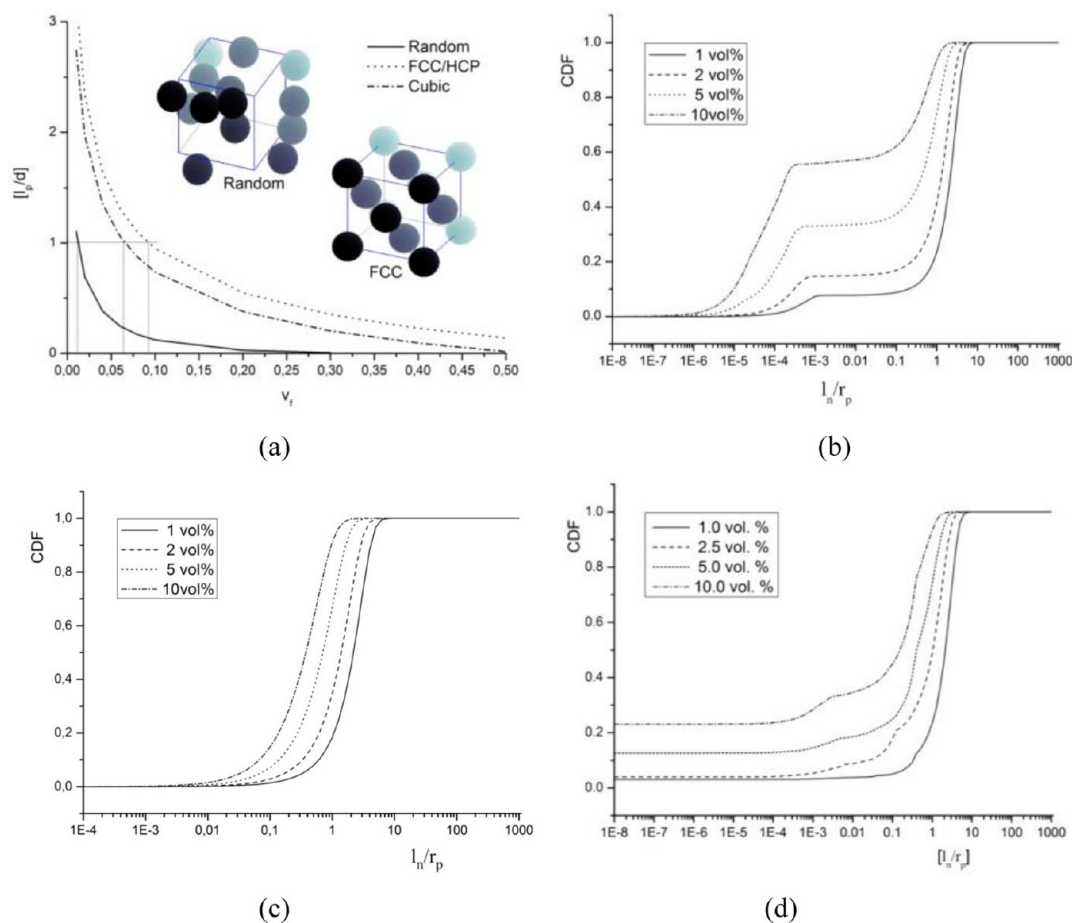


Figure 4. (a) Dependence of the shortest interparticle distance normalized to the NP diameter as a function of NP volume fraction, v_f , for random and regular spatial arrangement of monodisperse spheres. Cumulative distribution function (CDF) of the nearest interparticle distance (l_n) normalized to the particle radius (r_p) for the distribution of monodisperse spheres simulated using the model derived in ref 38. The CDF are shown for low mixing rate (b) and high mixing rate (c) prepared undeformed specimens. The CDF of the high mixing rate specimens subject to 1% compressive deformation is shown in part d, demonstrating the effect of the particle–particle interactions in formation of NP clusters during compressive loading.

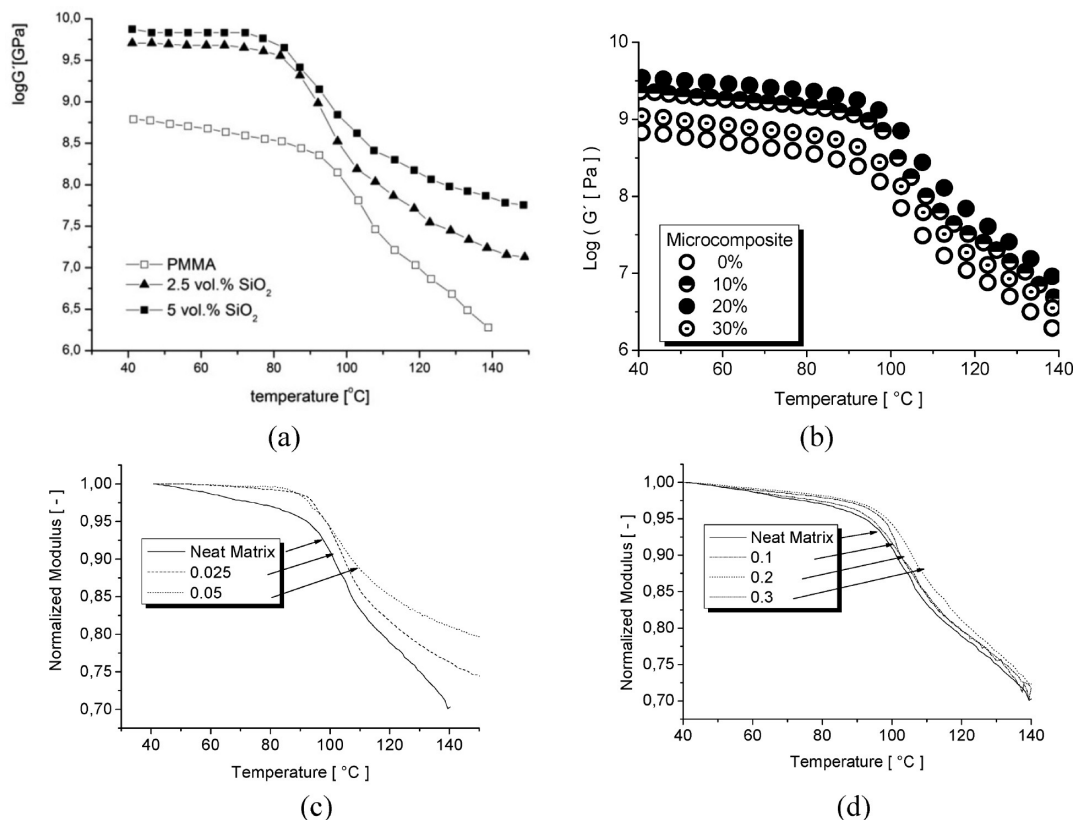


Figure 5. Temperature dependence of the logarithm of the storage shear modulus, $\log G'(T)$, for the PMMA (M_w) filled with (a) nanoparticles and (b) microparticles both measured using ARES DMA (TA, Inc., USA) at 1 Hz and at heating rate of 5 K/min. (c) Data from part a relative to the shear modulus at 40 °C; (d) data from part b relative to the shear modulus at 40 °C.

roughly equal to the R_g of the PMMA used (see Figure 3a). In randomly packed monodisperse systems, a significant shift in the average interparticle distance, l_p , toward shorter interparticle distances is observed when compared to a regular FCC spatial packing (which maximizes inter-NP distances at fixed v_f ; see Figure 4a).

It should also be noted that increasing the concentration of nanoparticles and altering the way NPs are mixed into the polymer both dramatically shift the cumulative distribution function (CDF) for the number of particles in contact (agglomerates). Simulation results show how both the number of particles contained in agglomerates (vertical shift in Figure 4b) as well as how rapidly particle spacing converges (horizontal shift in Figure 4c) increase with particle concentration. Compressive loading dramatically alters the interparticle distributions, as shown in Figure 4d. Even at very small strains of order 1%, a clear “shoulder” develops as some particles are brought into contact. Note that Figure 4 presents results for hard-sphere repulsive NPs. Since silica particles possess attractive interactions, the distributions of NPs will be quantitatively different in a real PMMA–SiO₂ composite, but we expect that Figure 4 provides a useful description of trends, and use it to analyze the results presented below.

As discussed above, a key parameter for mechanical response in the current investigation is $T_g - T$. We now characterize how NPs affect the linear rheology and glass transition behavior of our samples using DMA. In these measurements, we assume that macroscopic response is obtained by averaging over the effects of NPs, with the details of the averaging process assumed to be unimportant. It is generally accepted that the chain dynamics in the “glassy layer” near NP surfaces are slower than that in the

polymer bulk due to the inability of the chain to sample the whole conformation space. If a sufficiently large volume of chains exhibits modified dynamics, change in the glass transition temperature, T_g , may result.^{39,40} In the literature, one can find both upward,⁴¹ downward,^{42,43} or negligible^{44,45} shifts of T_g for the same systems; our observations are consistent with the second of these.

Figure 5 shows the temperature dependence of the storage modulus G' . Values of T_g were determined from the temperature dependence of the storage shear modulus, $G'(T)$, as the inflection point of the $\log G'(T)$ dependence. Adding up to 5 vol % of SiO₂ results in only a slight reduction of T_g (~ 4 K) when compared to the neat PMMA (Figure 5c). This shift is within the range of the accuracy of the DMA measurements and the reproducibility of sample preparation. We believe that this small shift produces only secondary effects for the measurements of primary interest in this study (made at temperatures at least 20 K below T_g , and focusing on $G_H - \sigma_{yr} - \nu_f - S_f$ relationships). No measurable change in T_g was observed in the case of MP filled PMMA (Figure 5b). We therefore make the *approximation* that T_g is independent of both the micro and nano filler volume fraction, v_f , and use the value for neat PMMA (373 K) as a reference T_g for measurements of temperature-dependent properties in the glassy state. Another, practical reason for adopting this convention is that no generally accepted theory satisfactorily elucidating *small* v_f -dependent changes in T_g has yet been published. Further, the results we report below contrast the response at $T_{hi} = T_g - 20$ K with the response at $T_{lo} = T_g - 80$ K; we do not believe that the effects of small v_f -dependent shifts in T_g shown in Figure 7 are critical here, since differences in response are expected to depend only on the *order of magnitude* of $(T_g - T_{lo})/(T_g - T_{hi})$.

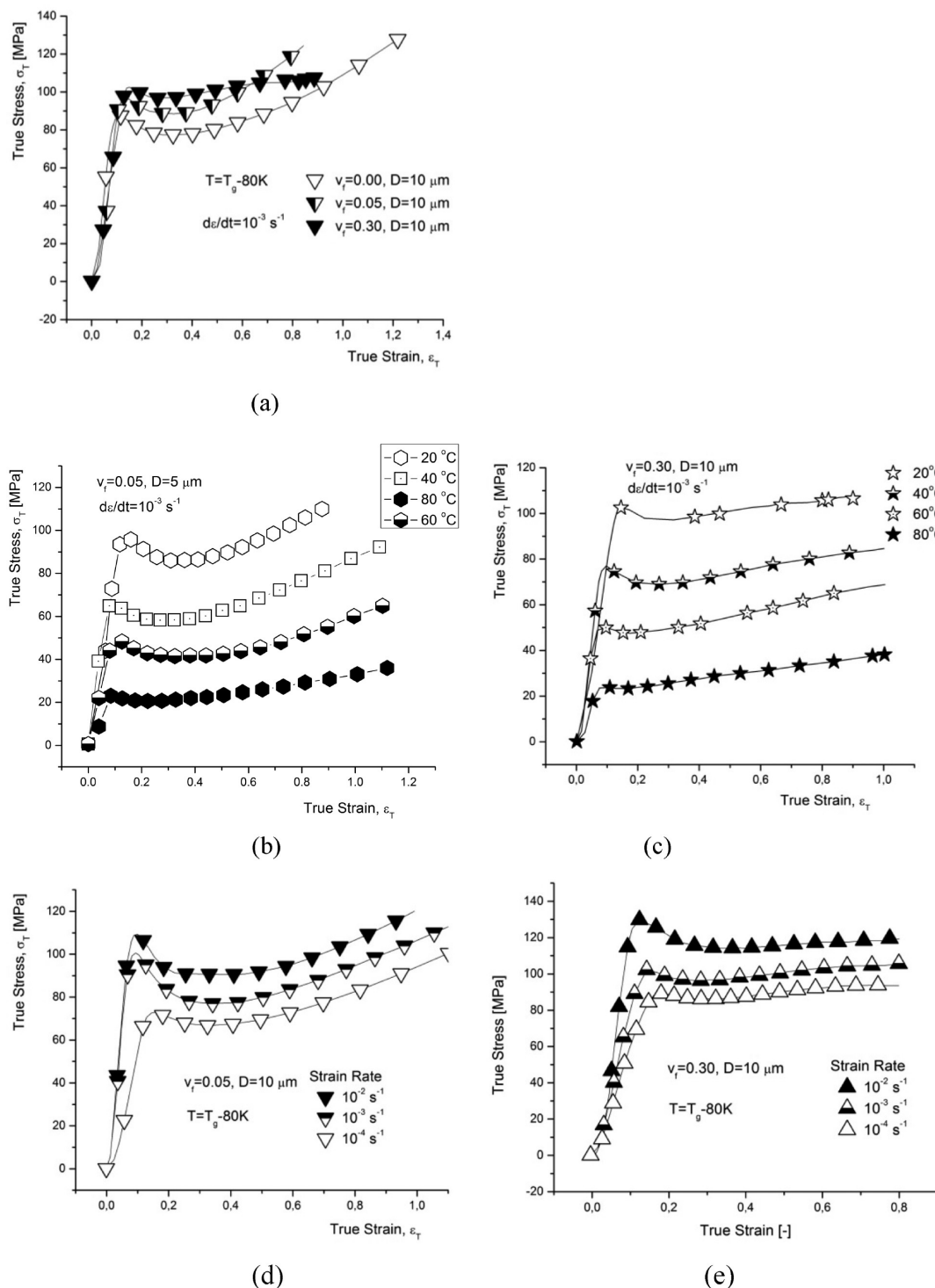


Figure 6. Characteristic $\sigma_T - \epsilon_T$ curves for (a) PMMA/fused SiO_2 beads composites at different v_f at the strain rate of 10^{-3} s^{-1} and $T_{L0} = T_g - 80 \text{ K}$, (b) for the PMMA filled with 5 vol % of fused SiO_2 beads over a range of temperatures between T_{L0} and T_{hi} at the strain rate of 10^{-3} s^{-1} , (c) for the PMMA filled with 30 vol % of fused SiO_2 beads over a range of temperatures between T_{L0} and T_{hi} at the strain rate of 10^{-3} s^{-1} , (d) for the PMMA filled with 5 vol % of fused SiO_2 beads over a range of range of strain rates at $T_{L0} = T_g - 80 \text{ K}$, and (e) for the PMMA filled with 30 vol % of fused SiO_2 beads over a range of range of strain rates at $T_{L0} = T_g - 80 \text{ K}$.

However, we use the data presented in Figure 5, parts a and b, as follows. From the significant reduction of the strength of the temperature dependence of G' near T_g upon addition of the nanosized SiO_2 (Figure 5a) one can conclude that the NPs reduce the system fragility significantly, analogous to antiplasticizers.²² We argue below that this effect is associated with increasing spatial and dynamic heterogeneities.⁵¹ Unlike for the

nanofilled PMMA, the fragility remains almost unaffected in the case of microfilled PMMA in agreement with the assumed negligible volume of the interface affected segments. This provides further support to the hypothesis of the role of the specific particle–PMMA interface area, S_p , in controlling the amount of particle affected chain segments (reduced mobility, modified packing).

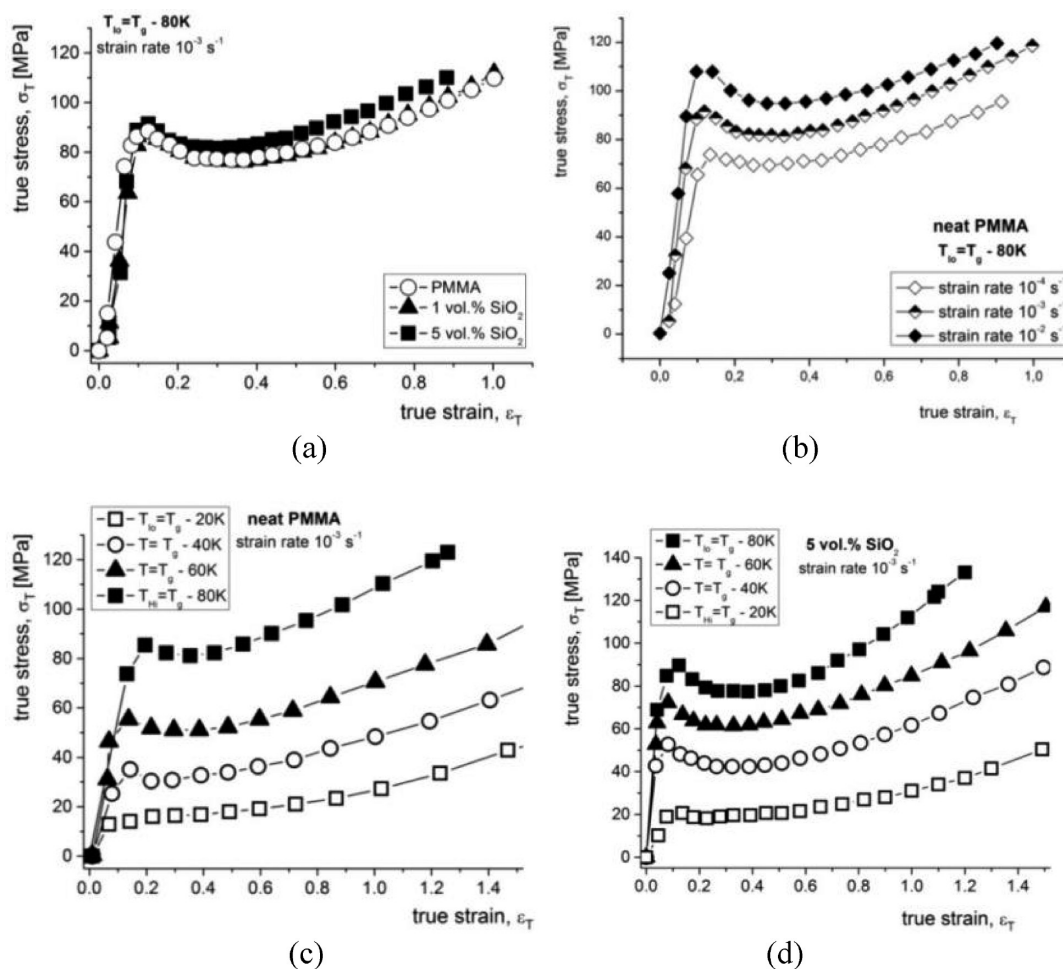


Figure 7. Characteristic $\sigma_T - \epsilon_T$ curves for (a) PMMA/SiO₂ nanocomposites at different SiO₂ concentrations at the strain rate of 10^{-3} s^{-1} and $T_{lo} = T_g - 80 \text{ K}$, (b) for the neat PMMA over a range of strain rates at $T_{lo} = T_g - 80 \text{ K}$, (c) for the neat PMMA over a range of temperatures between T_{lo} and T_{hi} at the strain rate of 10^{-2} s^{-1} , and (d) the same as in part c for PMMA/SiO₂ with $\nu_f = 0.05$.

Before turning to the main focus of this paper—the plastic flow and strain hardening regimes—we briefly present results for the entire range of mechanical response. Representative true stress - true strain ($\sigma_T - \epsilon_T$) curves are shown in Figures 6 (microfilled) and 7 (nanofilled) for varying strain rate, temperature, and ν_f . Panel a in Figure 6 exhibits data for different microfiller volume fractions at the strain rate of 10^{-3} s^{-1} at T_{Lo} . Data for different temperatures at the same low strain rate are shown in panels b (5 vol %) and c (30 vol %) of Figure 6. Finally, data for different strain rates at T_{Lo} are presented in panels d (5 vol %) and e (30 vol %) of Figure 6. Adding more than 20 vol % of MPs resulted in fracture of the specimens prior to developing strain hardening region of desired size at $T_g - 80 \text{ K}$ (Figure 4, parts a, c, and e). Thus, the strain hardening modulus, G_{Hb} , determined for 30 vol % MP filled PMMA carries a large experimental uncertainty. Note that the effects of thermal history on the large strain deformation response for MP filled PMMA within the ν_f temperature and strain rate intervals used were insignificant. Hence, we present data only for annealed microcomposites.

For nanofillers, Figure 7a presents data for different silica loading fractions at a single (low) strain rate at $T = T_{lo}$. There is little measurable difference in the postyield regime between neat PMMA and nanocomposites with $\nu_f = 0.01$. However, at higher nanoparticle concentrations ($\nu_f = 0.05$), a pronounced increase

in the yield and flow stresses is observed. Panels b and c of Figure 5 show pronounced rate and temperature effects for neat systems; these are further examined below via kinetic analyses. Interestingly, the $\nu_f = 0.01$ and $\nu_f = 0.05$ curves are not parallel at large strains (panel b). Within the Eyring-like picture of ref 5, this would indicate a strain-dependent activation volume V^* (i.e., V^* increases at large strains), which is reasonable considering the changes in inter-NP correlations expected at large strains (Figure 4). Panels c and d of Figure 7 contrast the temperature dependences of the response for neat and $\nu_f = 0.05$ systems. Adding SiO₂ filler produces marked changes in the shapes of the stress-strain curves, especially for $T = T_{lo}$. For example, silica-filled systems show a significantly more pronounced yield drop. More will be detailed regarding these effects in an upcoming publication, and in the following discussion.

Note that in NP-filled systems, the value of the specific interface area (S_f) is much larger than could be obtained with micrometer-sized fillers at similar loading; many studies have shown that the large ratio of S_f to filler volume produces effects on mechanical properties that can be obtained only at far higher loadings of micrometer-size particles. In Figure 8a, we present values of the composite modulus, $E_c(\nu_f)$, relative to the matrix modulus, $E_m(0)$, i.e., $E_c^{rel} = E_c(\nu_f)/E_m(0)$. The E_c^{rel} values increase sharply with increasing ν_f and the increase is much more dramatic for nanoparticles. Figures 8b (below T_g) and 8c

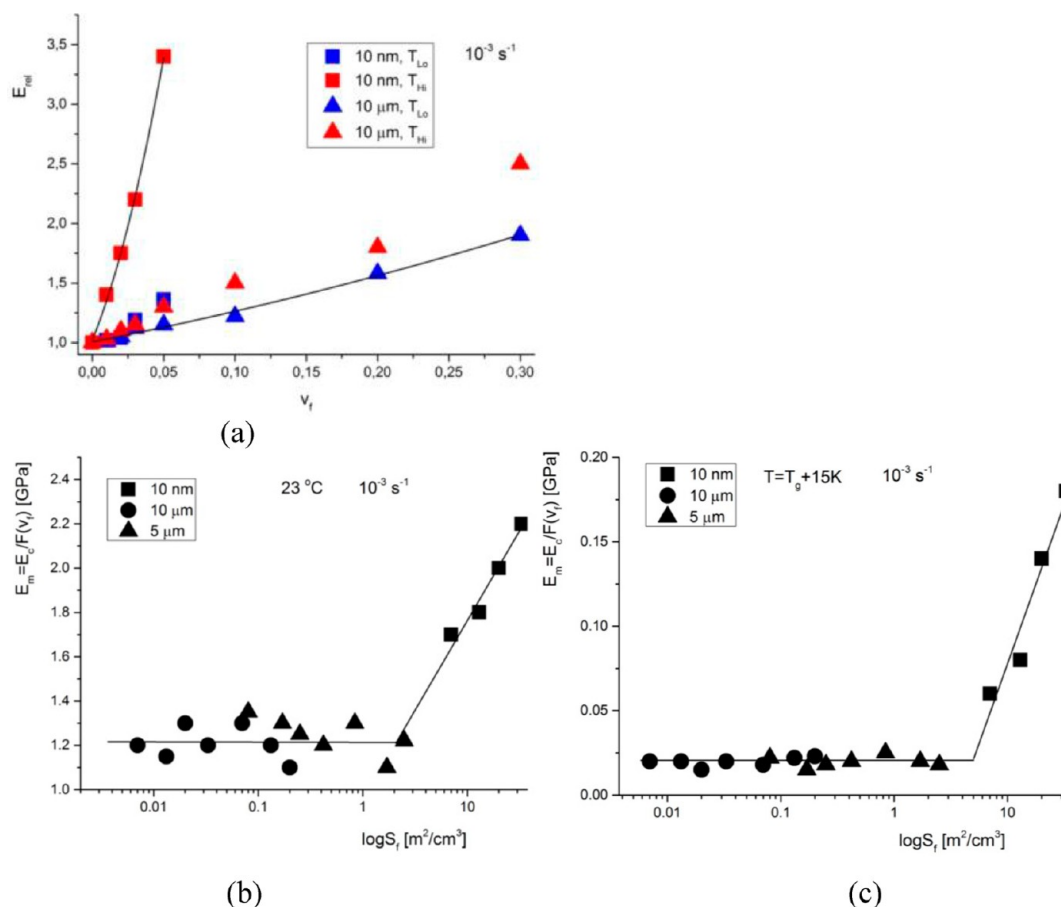


Figure 8. Plot of the composite modulus, E_c relative to that of the neat PMMA as the function of filler volume fraction, v_f , at T_{Lo} and T_{Hi} (a) and plot of the matrix modulus, E_m , as a function of the specific interface area per 1 cm^3 of the micrometer and nanometer particle filled PMMA at (b) $T = T_g - 80 \text{ K}$ and (c) $T = T_g + 15 \text{ K}$ measured at strain rate of 10^{-3} s^{-1} . Fused SiO_2 microfiller (Figure 2e) was used in these measurements as the $5 \mu\text{m}$ filler.

(above T_g) show the plots of the matrix modulus, E_m , normalized by the volume replacement function $F(v_f)$, i.e., $E_m = E_c/F(v_f)$, on the S_f per 1 cm^3 of the composite. The reinforcement of the particulate filled amorphous polymer consists of a contribution related to the (i) volume of the rigid filler, (ii) contribution due to the molecular stiffening caused by the interaction between particle surface and matrix chains, and (iii) stress transfer due to shear stress at the matrix–filler interface. The stress–transfer contribution is negligible in composites with spherical fillers. The filler–volume contribution dominates for particles with small surface to volume ratio (MPs) while the surface interaction contribution dominates for particles with large surface to volume ratio (NPs). Commonly used models inherently assume that the matrix modulus is independent of particle content and size,⁴⁹ i.e., $E_m(v_f) = E_m^0 = \text{const}$. For simplicity, a modified Einstein–Bachelor law³⁶ (eq 5), describing the pure volume replacement contribution to composite stiffening ($F(v_f)$) was used⁴⁹ to calculate the E_m . Neat PMMA exhibited $E_m^0 = 1.3 \text{ GPa}$ at T_{Lo} and 0.02 GPa at $T = T_g + 15 \text{ K}$.

The use of S_f as the structural variable allows to separate the effect of the PMMA–particle interface area from the volume replacement contribution. For the MP-filled composite, $E_m \approx E_m^0$ remained independent of S_f over the entire composition interval investigated as assumed in the classical composite micromechanics. For NP filled composites, however, approximately exponential growth of E_m with S_f was observed at both temperatures in agreement with published data.⁴⁹ This result is important for further considerations of the differences in effects

caused by micro- and nanometer sized filler particles. The amount of chains affected by the NP particle surface is several orders of magnitude larger compared to MP particles (with similar strength interfacial interactions) even at high v_f of MPs.

We now turn to the main focus of this paper—the plastic flow and strain hardening regimes of glassy PMMA composites. We begin by reporting values for the yield and rejuvenated yield (i.e., our best approximation of “true” plastic flow) stresses, in Table 1 Values of σ_y depend strongly on the preparation protocol as expected, i.e., are larger for annealed systems, while quenched and annealed systems have almost identical σ_{yr} within our experimental accuracy. Typical true stress–strain curves for annealed microfilled PMMA and for annealed and quenched nanofilled systems are shown in Figures 6 and 7, respectively.

One unusual result is that the values of G_H for quenched (and unaged) systems are systematically smaller than those for the annealed (and aged) systems, especially for the NP-filled systems. This contradicts the generally observed result³ that strain hardening is independent of thermal history, i.e., values of G_H should be independent of preparation protocol. There are several potential interpretations for our finding of systematically smaller G_H in quenched systems. The simplest is that since our chains are rather short (SM_c), disentanglement occurs during deformation in the strain hardening regime and is faster in quenched systems compared to annealed systems because quenched systems lie higher on their energy landscape,⁴⁶ reducing the activation energy for disentanglement. Another interpretation is more local: upon annealing, stronger “caging”

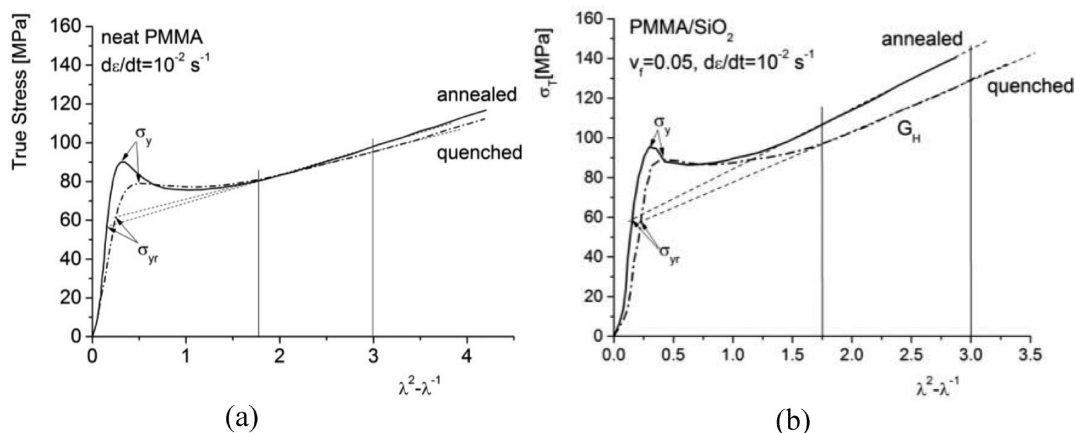


Figure 9. True stress–neo-Hookean strain curves for annealed and quenched neat PMMA (a) and PMMA/SiO₂ (b) specimens measured at T_{lo} and strain rate of 10^{-2} s^{-1} .

occurs or, in other words, the segments fall into deeper free energy wells compared to the quenched ones, so enhancing their mobility under applied strain requires more energy. The PNLE theory suggests¹⁹ that the amplitude of density fluctuations (which controls strain hardening¹⁷) would be larger for annealed/aged systems. In any case, preparation-protocol-dependence of strain hardening in weakly entangled systems has not, to our knowledge, been previously investigated, and we do not believe our findings of larger G_H in annealed systems contradict any published results.

The greater preparation-protocol-dependent difference in G_H for filled systems (Figure 9b) is less surprising. The relaxation time associated with the segment interfacial adsorption–desorption process, τ_R , can be assumed to be exponential in the chain-particle interaction strength. During the annealing process at elevated temperature, there is more time for segments close to NPs to more efficiently pack, and thus the NPs both (i) more significantly retard segmental dynamics in the interfacial area and (ii) act as more effective entanglement attractors. It has previously been shown³² that the entanglement-attractor effect of nanoparticles is particularly important at large deformations, but the ways in which preparation protocol alters such effects has not previously been investigated.

One way of validating the above assertions regarding preparation-protocol dependence is to perform kinetic analyses that identify characteristic activation energies for plastic flow and strain hardening. We will show that annealed systems possess slightly larger activation energies for both G_H and σ_{yr} . Since PMMA at temperatures between T_{lo} and T_{hi} exhibits thermorheological complexity, a Ree–Eyring analysis is required. We use the Ree–Eyring model^{48,61} in the form proposed by Roetling⁴⁷ to analyze the flow behavior of our systems. Replacing the standard analysis of yield stress with one of rejuvenated yield stress yields:

$$\frac{\sigma_{yr}}{T} = \sum_i \frac{1}{A_i} \sinh^{-1} \left\{ \frac{C_i}{T} \frac{d\epsilon}{dt} \exp \left(\frac{\Delta U_i}{RT} \right) \right\} \quad (1)$$

where A_i , C_i , and ΔU_i are constants for the individual relaxation processes involved ($i = 1, 2$). Van Breemen et al.⁶² assumed the values of i corresponded to additive α - and β -relaxation processes and obtained a (mathematically) equivalent form for the yield stress of rheologically complex PMMA. Replacing the yield stress with the rejuvenated yield stress yields:

$$\frac{\sigma_{yr}}{T} = \left[\frac{k_B}{V_\alpha} \sinh^{-1} \left(\frac{\frac{d\epsilon}{dt}}{\frac{d\epsilon_{0,\alpha}}{dt} \exp \left(-\frac{\Delta U_\alpha}{RT} \right)} \right) \right] + \left[\frac{k_B}{V_\beta} \sinh^{-1} \left(\frac{\frac{d\epsilon}{dt}}{\frac{d\epsilon_{0,\beta}}{dt} \exp \left(-\frac{\Delta U_\beta}{RT} \right)} \right) \right] \quad (2)$$

V_α , V_β , ΔU_α and ΔU_β represent activation volumes and energies for the independently acting α - and β -relaxations, $d\epsilon_{0,\alpha}/dt$ is the rate constant for the α process, and $d\epsilon_{0,\beta}/dt$ is the rate constant for the β process.

We are not aware of any previous detailed kinetic analyses of strain hardening in either neat, micro or nano composite systems. We assume that the same theoretical framework as described above can be used to analyze the kinetics of the reduced strain hardening modulus G_H/T :

$$\frac{G_H}{T} = \left[\frac{k_B}{V_\alpha^*} \sinh^{-1} \left(\frac{\frac{d\epsilon}{dt}}{\frac{d\epsilon_{0,\alpha}}{dt} \exp \left(-\frac{\Delta U_\alpha^*}{RT} \right)} \right) \right] + \left[\frac{k_B}{V_\beta^*} \sinh^{-1} \left(\frac{\frac{d\epsilon}{dt}}{\frac{d\epsilon_{0,\beta}}{dt} \exp \left(-\frac{\Delta U_\beta^*}{RT} \right)} \right) \right] \quad (3)$$

Note that while G_H is a modulus rather than a scalar stress, it has the same dimensions as stress and may be analyzed within an Ree–Eyring model framework. We show below that such an analysis is meaningful. V_α^* , V_β^* , ΔU_α^* , and ΔU_β^* represent activation volumes and energies for the independently acting α and β relaxations in the strain hardening regime.

The activation energies and volumes of the individual α and β relaxation processes for rejuvenated yield and strain hardening are given in Tables 2 and 3, respectively, and were obtained by fitting experimental data (Figures 10 and 11) to eqs 2 and 3. Since the arguments X of the $\sinh^{-1}(X)$ functions in eqs 2 and 3 are large, we made the standard approximation $\sinh(X) = 1/2[\exp(X)]$.

Previous Ree–Eyring analyses of yield stress in glassy polymers have fit thermal-history-dependent variations by varying the

Table 2. Parameters of the Ree–Eyring Model for Neat PMMA, NP, and MP-Filled PMMA Obtained by Fitting Experimental Data with Eq 2^a

thermal history	filler	ν_f	V_{α}^* [nm ³]	ΔU_{α}^* [kJ mol ⁻¹]	V_{β}^* [nm ³]	ΔU_{β}^* [kJ mol ⁻¹]
Q	none	0	0.82	191	0.98	85
A	none	0	0.85	200	1.01	89
Q	10 nm	0.01	0.87	200	1.02	89
A	10 nm	0.01	0.88	205	1.03	93
Q	10 nm	0.05	0.89	232	1.03	95
A	10 nm	0.05	0.94	228	1.03	95
A	10 μ m	0.01	0.82	200	0.98	89
A	10 μ m	0.05	0.85	205	1.00	90
A	10 μ m	0.30	0.91	220	1.05	98

^aNo measurable difference was observed between quenched and annealed microcomposites; hence, only data for annealed microcomposites are shown. For all systems, $d\epsilon_{0,\alpha}/dt$ and $d\epsilon_{0,\beta}/dt$ were respectively $6 \times 10^{25} \text{ s}^{-1}$ and $3.2 \times 10^{13} \text{ s}^{-1}$.

Table 3. Parameters of the Ree–Eyring Model for Neat PMMA, NP, and MP-Filled PMMA Obtained by Fitting Experimental Data with Eq 3^a

thermal history	filler	ν_f	V_{α}^* [nm ³]	ΔU_{α}^* [kJ mol ⁻¹]	V_{β}^* [nm ³]	ΔU_{β}^* [kJ mol ⁻¹]
Q	NA	0	3.82	202	1.20	89
A	NA	0	3.75	204	1.22	89
Q	10 nm	0.01	3.94	212	1.31	90
A	10 nm	0.01	3.90	216	1.33	90
Q	10 nm	0.05	4.62	228	1.35	93
A	10 nm	0.05	3.94	232	1.35	94
A	10 μ m	0.01	3.82	204	1.28	89
A	10 μ m	0.05	3.85	205	1.20	90
A	10 μ m	0.30	3.91	216	1.25	93

^aNo measurable difference was observed between quenched and annealed microcomposites; hence, only data for annealed microcomposites are shown. For all systems, $d\epsilon_{0,\alpha}/dt$ and $d\epsilon_{0,\beta}/dt$ were respectively $6 \times 10^{25} \text{ s}^{-1}$ and $3 \times 10^{13} \text{ s}^{-1}$.

associated rate constants. We likewise obtain similarly good fits to our data by varying these. However, one inherent feature of multiparameter, phenomenological fitting models like the Ree–Eyring equation is the possibility of obtaining similarly good fits of experimental data by varying different parameters.⁶⁸ When this occurs, it is not at all clear which parameters *should* be varied, and the previous groups' choice to vary the rate constants is only one out of two choices that are equally valid given current knowledge of the microphysics of these systems. In our analysis, where all the 4 parameters were varied, the α -process rate constant varied within 1 order of magnitude between 5×10^{36} and $6 \times 10^{37} \text{ s}^{-1}$ over the entire ranges of composition and thermal history employed; this represents a fractional variation of only 10^{-36} . Similarly for the β -process, the rate constant varied between 2×10^{12} and $3.2 \times 10^{13} \text{ s}^{-1}$, representing a fractional variation of only 10^{-12} . These variations are negligible. In contrast, the fractional variations of the activation volume for the α -process and β -process due to thermal history or composition were respectively of order 10–20% and 1–3%. We consider these variations much more relevant for interpretation of our experimental data. Physically, we interpret the rate of a relaxation process as being dependent on the position of a system on its energy landscape, i.e. on its thermal history. Alternatively, however, one can view the effects of thermal history on this positioning as a change of the

activation volume relevant to the relaxations that must occur to facilitate plastic flow. We choose the latter approach in our interpretation of the data for the PMMA used in our experiments since it may better suit the apparent nanoscale structural heterogeneity of PMMA.

The obtained Ree–Eyring parameters for the flow stress of neat PMMA agree fairly well with previously published results for the yield stress.^{47,62,63,65,68} Differences are of order 20% and may be attributed to the fact that we analyzed the mechanically rejuvenated yield stress σ_{yr} whereas most previous authors analyzed the yield stress σ_y (see Figure 9) or the flow stress (as measured by the postyield minima of stress–strain curves), to differences in chain tacticity, or to the rather small molecular weight of PMMA employed here (about 1/3 of that employed by Roetling⁴⁷). Van Breemen et al. observed⁶² that at 20 °C, above the strain rate of 10^{-3} s^{-1} , there is a gradual increase in the amount of strain softening with increasing strain rate. The kinetics of the upper (σ_y) and lower (σ_{yr}) yield stress are different at these strain rates, leading them to conclude that this increase is attributable to kinetics of yield being controlled by both α - and β -relaxations while the kinetics of the flow stress being controlled only by the α process. Our results are consistent with this conclusion; in our studied temperature range, the contribution of the β process to rejuvenated yield stress is only a few percent. Contributions of the β process to strain hardening are also at the few-percent level, supporting the use of coarse-grained modeling approaches that treat only α (segmental-scale) physics, such as PNLE theory and/or bead–spring simulations, to understand plastic flow and strain hardening in polymer glasses in nanocomposites.

The main outcome of the Ree–Eyring analyses (Tables 2 and 3) is that there are no substantial differences between the activation energies for rejuvenated yielding and strain hardening for the any of the systems investigated. However, values of the activation volumes for the α process are about 4 times larger for strain hardening than for plastic flow. This is consistent with the idea that strain hardening mobilizes a larger volume;³¹ the amount of material which must be plastically deformed in order to maintain chain connectivity increases with increasing strain. The observation that the alpha process appears to control both flow and hardening under the conditions employed here also supports recent theoretical predictions^{11,17,30,31} as well as experimental observations¹³ that flow and hardening scale with one another and are controlled by similar processes. Below, we test this idea further, and identify the factors which (similarly) affect flow and hardening with increasing ν_f . To conclude our focus on kinetic analysis of the α process, results in Table 3 support our above contention that the preparation-protocol-dependent G_H we have observed above arises from quenched and annealed systems occupying different positions on their energy landscape.^{58–60} For all ν_f values of ΔU_{α}^* are larger for annealed than for quenched systems, while values of V_{α}^* are smaller. These trends are consistent with the idea that annealed systems possess tighter⁶⁶ segmental packing. Tighter segmental packing in annealed systems would increase the amount of material which has to be mobilized in order to produce plastic flow while maintaining chain connectivity. If this is true, one would expect (from PNLE theory^{16–19}): (i) greater retardation of segmental dynamics, (ii) amplified density fluctuations, (iii) larger absolute values of G_H and (iv) greater rate dependence of G_H at $T = T_{Hv}$ resulting in (v) breakdown of volume-replacement models that account only for hard-sphere-like interactions between NPs and the polymer matrix. We have shown above that trends (iii and iv)

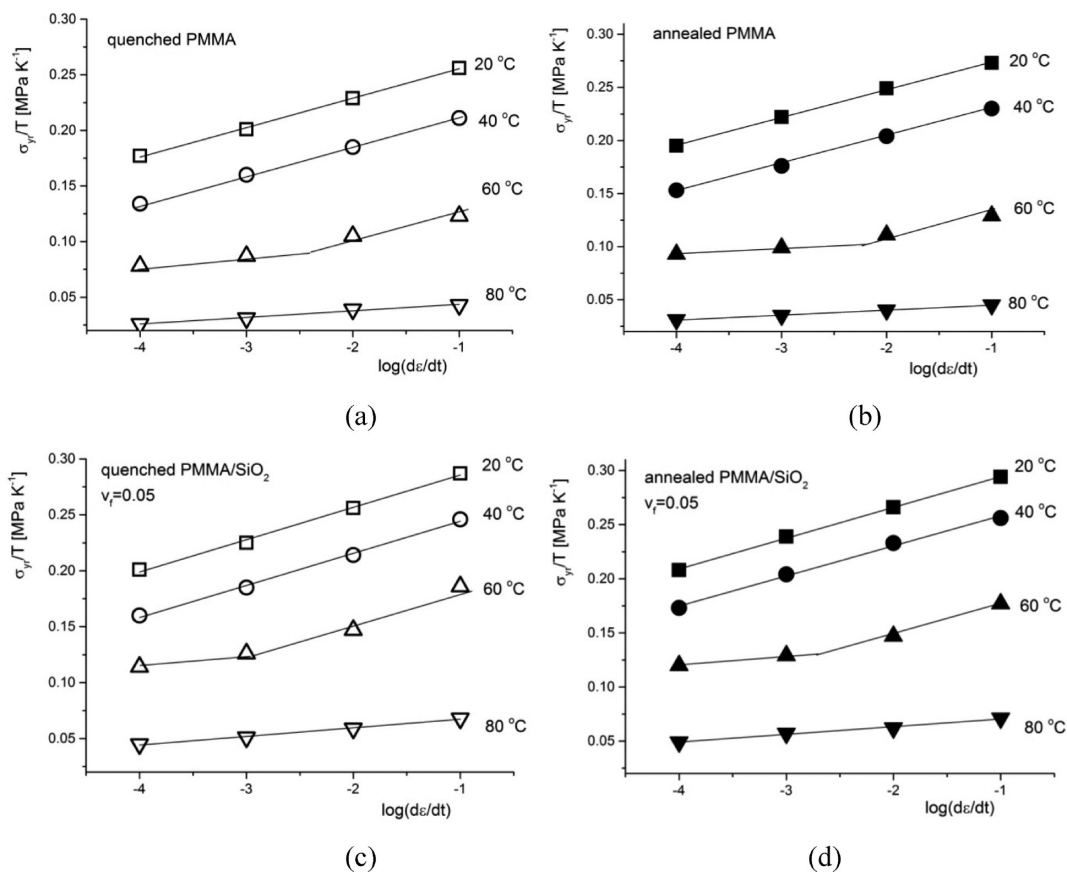


Figure 10. Ree–Eyring plots of (a) the reduced mechanically rejuvenated yield stress σ_{yr}/T , for (a) quenched PMMA, (b) annealed PMMA, (c) quenched SiO₂-filled PMMA ($v_f = 0.05$), and (d) annealed SiO₂ filled PMMA ($v_f = 0.05$).

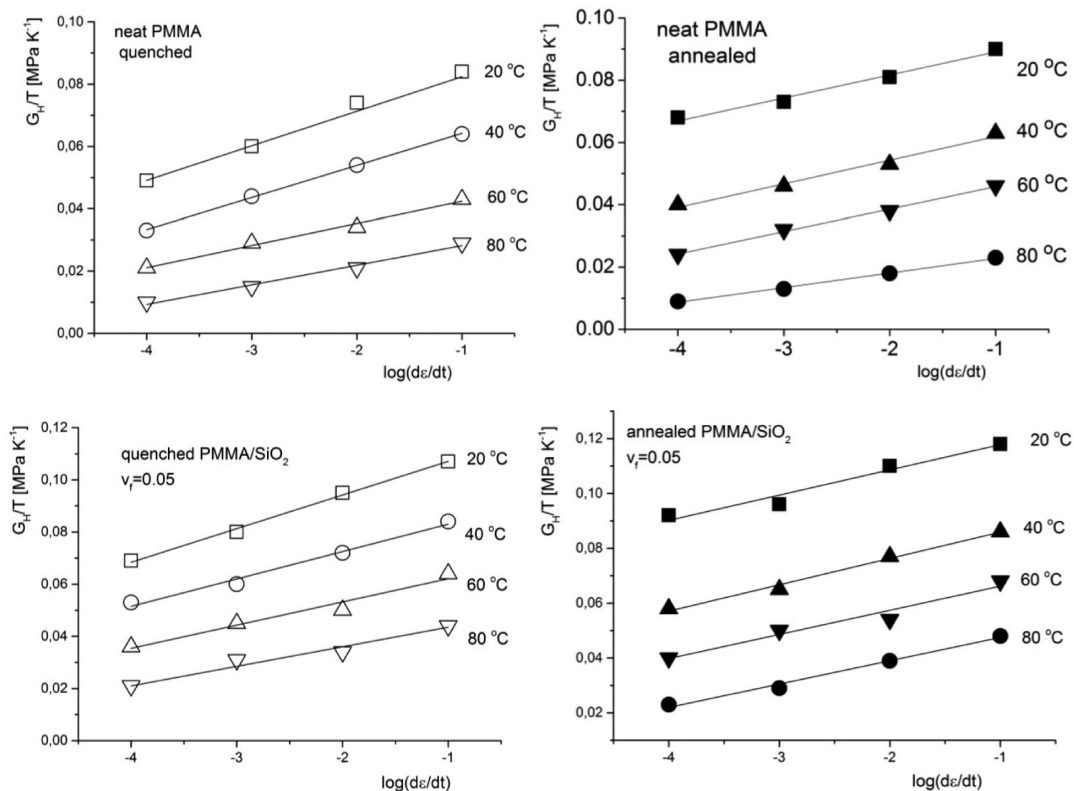


Figure 11. Ree–Eyring plots of (a) the reduced (here “reduced” refers to division by temperature) strain hardening modulus, G_H/T , for (a) quenched PMMA, (b) annealed PMMA, (c) quenched SiO₂ filled PMMA ($v_f = 0.05$) and (d) annealed SiO₂ filled PMMA ($v_f = 0.05$).

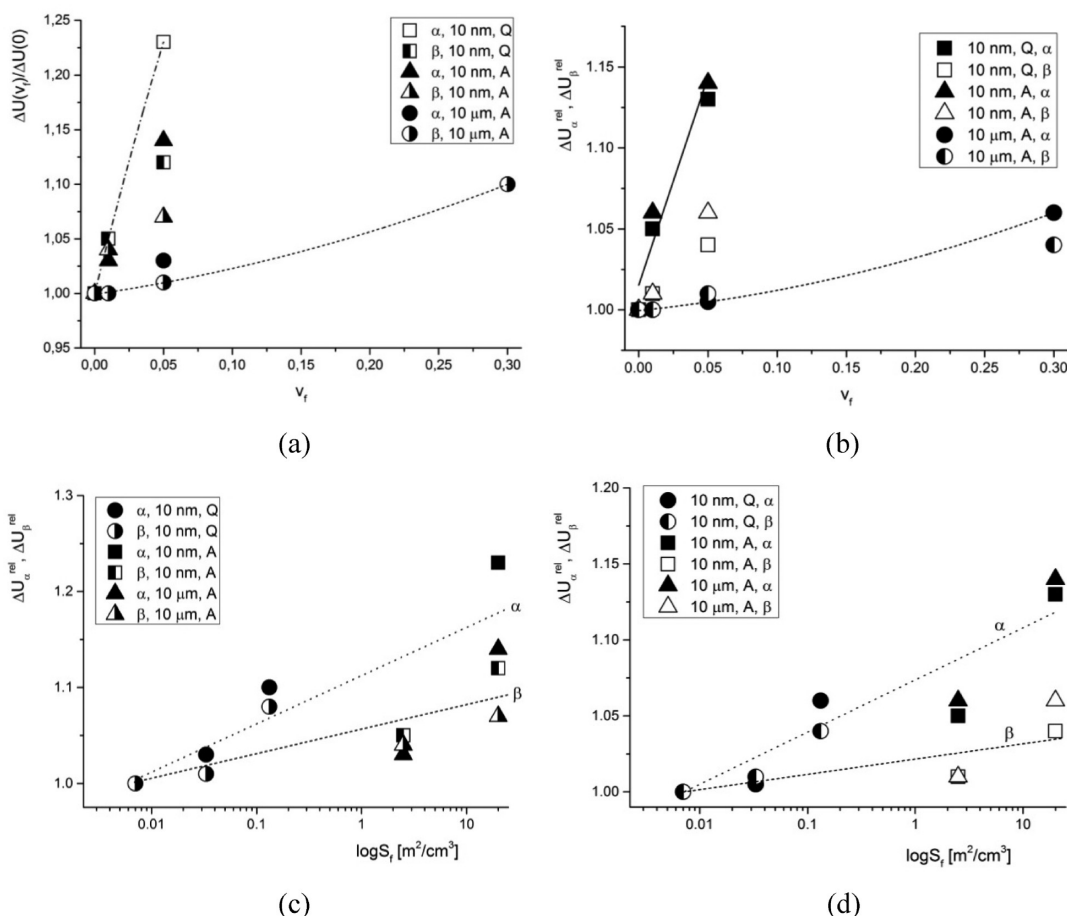


Figure 12. Plots of the activation energy of the α and β processes for the NP and MP filled PMMA relative to those for neat PMMA (both quenched and annealed as appropriate) for the yielding (a) and strain hardening (b) regimes. Plots of relative activation energies, ΔU^{rel} , for both processes as a function of the $\log S_f$ for (c) rejuvenated yielding and (d) strain hardening. Lines serve as guides for the eyes only.

are indeed observed, and we will show below that trend v is observed, forming a consistent picture. However, we strongly emphasize that the above-reported preparation-protocol dependence of G_H does not qualitatively change any of the key results reported below: applicability of volume-replacement models for G_H , and scaling relationships between G_H and σ_{yr} .

Next we analyze the ν_f -dependence of the data in Figures 10–11 and Tables 2–3. For convenience, values of activation energies, $\Delta U(\nu_f)$, relative to that for neat PMMA, $\Delta U(0)$, are plotted in Figure 12 for both α and β process, for micro- and nano-filled systems both quenched and annealed. Figures 12a and 12b respectively depict results of our Ree–Eyring analyses of the rejuvenated yield stresses and strain hardening moduli. The interpretation of the increase in ΔU_α with increasing ν_f is straightforward and intuitive; weakly attractive SiO_2 –PMMA interactions should increase the energy required to activate the segmental rearrangements associated with plastic flow. As already reported^{49,67} and shown in Figure 8, the amount of chains affected by the presence of rigid weakly attractively interacting particles is proportional to the specific interface area in per unit volume of the composite, S_f . This seems to be valid also for rejuvenated yielding (Figure 12c) and strain hardening (Figure 12d). Unlike for the nanocomposites, in microcomposites, no measurable effect of thermal history was observed which further supports interpretation put forward above. This justifies our use on NPs as “probes” of the local segmental dynamics and packing in PMMA. Moreover, our results confirm

that the effect of rigid particles is more pronounced for the α process (involving the entire backbone chain) compared to the β process (presumably involving only few segments). Still further, it also seems that the NPs are slightly enhancing the contribution of the β process to the overall value of G_H . This is in agreement with our hypothesis of the heterogeneous distribution of relaxation mechanisms in NP filled PMMA brought about by the differences in behavior between bulk and interfacial chains.

Figure 13 shows the Ree–Eyring plots for σ_{yr}/T and G_H/T for the two characteristic temperatures T_{lo} and T_{hi} . We found no evidence of rheological complexity at these two temperatures. The main effect of both the MPs and NPs consisted of vertical upward shift of the $\sigma_{yr}/T - \log(d\epsilon/dt)$ and $G_H/T - \log(d\epsilon/dt)$ dependences in our $\log(d\epsilon/dt)$ “experimental window”, without affecting their slopes. According to the Ree–Eyring model,^{47,61} the vertical shift expressed by the constant C_i from eq 1 is related to the changes in entropy during the relaxations; this hypothesis qualitatively agrees with other results reported here.

Recalling Figure 3, one may consider the composite a three-phase system consisting of bulk PMMA chains, rigid underformable particles that do not contribute to relaxation, and interfacial PMMA chains with retarded dynamics and modified packing. At given values of T and $d\epsilon/dt$, the bulk chains exhibit the same relative contribution from the α and β relaxation as the neat PMMA under the same conditions. On the other hand, the interfacial chains exhibit filler-affected contributions from the

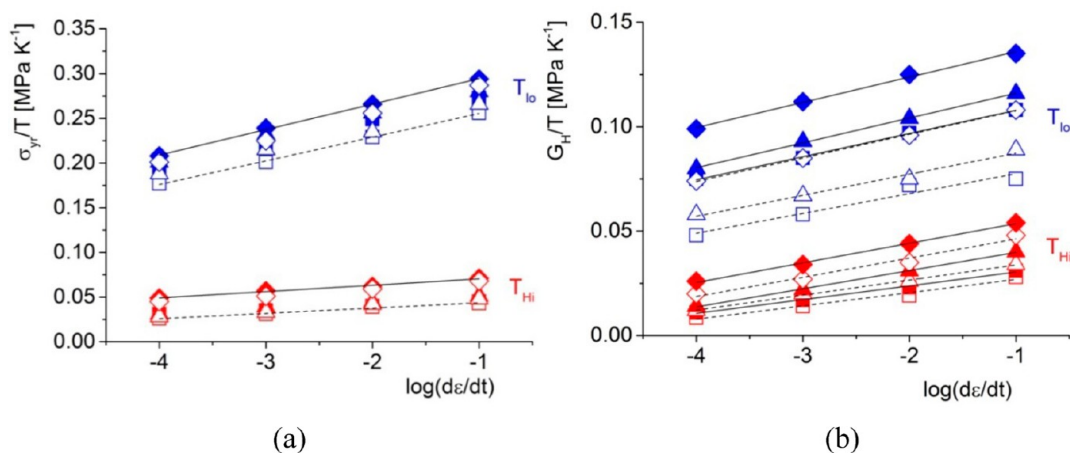


Figure 13. Ree–Eyring plots of (a) the reduced mechanically rejuvenated yield stress σ_{yr}/T , and (b) the reduced strain hardening modulus G_H/T , for quenched (open symbols) and annealed (filled symbols) PMMA and SiO₂ filled PMMA (squares for neat PMMA, triangles for $\nu_f = 0.01$, diamonds for $\nu_f = 0.05$), shown for $T_{lo} = T_g - 80$ K (blue) and $T_{hi} = T_g - 20$ K (red). Each of the rate dependences exhibits only a single temperature- and thermal-history-dependent slope.

α and β relaxations that we will show scale with ν_f or with the specific interface area S_f . Hence, these effects are more pronounced in NP filled PMMA compared to MP filled PMMA at the same ν_f .

Figure 13 also shows that for NP-filled systems, values of G_H increase monotonically with increasing ν_f . As for σ_{yr} , no evidence of rheological complexity of G_H is found at either T_{hi} or T_{lo} , providing further evidence that these two temperatures are suitable for analyzing both plastic flow and strain hardening in two characteristic, fundamentally different regimes. In all cases, and unlike results for flow stress, the rate dependence of the hardening modulus is stronger for annealed than for quenched systems. This curious result will be a topic for future studies. Below, we will provide evidence for the following interpretation of this result: at T_{hi} , the modified chain packing and retarded segmental dynamics near NP surfaces is much more important than at T_{lo} .

Previous work has shown⁴⁶ that the portion of PMMA chains with the SiO₂-retarded segmental dynamics and modified chain packing is proportional to the SiO₂–PMMA specific interfacial area per cm³ of the nanocomposite, S_f . At high frequencies (or temperatures far below T_g), the segmental dynamics in the vicinity of the SiO₂–PMMA interface does not differ substantially from that in the PMMA bulk. Also, the packing frustration is “frozen in” for both interface and bulk chains. Hence, the slow bulk chain dynamics dominates the deformational response of the nanocomposite. At low frequencies (or temperatures slightly below T_g), bulk chains exhibit substantially greater mobility compared to the SiO₂ interface-retarded chains. At the same time, the “frozen in” segmental packing frustration is released at a greater rate in the bulk compared to the surface-retarded region. Hence, the effect of the NP-surface-retarded segmental dynamics and packing frustration dominates the nanocomposites’ response to external deformation. In addition, the rate of sorption–desorption to/from nanoparticle surface is controlled by the NP-chain interaction energy. The number of segments in the chain N , nanoparticle size D , density of attractive interaction sites on the nanoparticle N_w , strength of the interaction ΔE , and ν_f were identified as the primary structural parameters affecting the sorption/desorption dynamics.³³ In agreement with these models, our experimental data suggest that the energy landscape in the quenched system at T_{lo} resembles that for the annealed system at T_{hi} .

To compare the microfilled and nanofilled systems, annealed and quenched at T_{lo} and T_{hi} , rejuvenated yield stresses and strain hardening moduli data relative to those for the neat PMMA, σ_{yr}^{rel} and G_H^{rel} , respectively, are presented in Figures 14 and 15. Our data in Figure 14a clearly show that the rejuvenated yield stress relative to that for the neat PMMA, σ_{yr}^{rel} , increases with ν_f for both micro- and nano-composites. The observed increase of σ_{yr}^{rel} with ν_f is steeper at T_{hi} compared to that at T_{lo} for both nanofilled and microfilled PMMA (Figure 14a). At T_{lo} , no significant difference is observed between quenched and annealed systems.

In the case of nanofilled PMMA, at T_{hi} , the annealed system exhibits significantly weaker ν_f dependence. This qualitatively corresponds with our hypothesis that presence of NPs increases the heterogeneity of the energy landscape and that the density of affected chain segments is proportional to the specific interface area. In annealed systems, this change would naturally be less pronounced due to the system lying in a deeper, more rugged portion of its energy landscape,⁴⁶ while in quenched systems which (in neat PMMA) have smoother energy landscapes, the presence of NPs causes a roughening of the landscape, i.e. deeper energy basins for interface-retarded segments.

In order to separate the volume replacement contribution, the σ_{yr}^{rel} was normalized to the volume replacement function, $F(\nu_f)$ (eq 5), to obtain σ_{yr}^{norm} (Figure 14b). The ν_f dependence of the relative yield stress is in reasonable agreement with observations of the rheological behavior of polymer melts containing rigid spherical nanoparticles.^{36,37} We compare the σ_{yr}^{rel} – ν_f dependences with a simple volume replacement model used to analyze the ν_f dependence of viscosity³⁶ or elastic modulus:⁴⁹

$$\sigma_y^{rel}(\nu_f) = F(\nu_f)$$

Our use of eq 3 is justified by the viscoplastic nature of stress in the flow regime, discussed further below. The volume replacement function $F(\nu_f)$ was assumed to take the form of a series expressed by the modified Einstein–Bachelor law:³⁶

$$F(\nu_f) = \sigma_y(\nu_f)/\sigma_{ym}(0) = 1 + (2.5k)\nu_f + P\nu_f^2 \quad (5)$$

Here $k \sim (R_g/D)^3$ describes the increase in the hydrodynamic size of the spherical particle due to the segment adsorption, and P is the NP-NP pair interaction coefficient.³⁶ For $\nu_f \geq 0.01$, the average interparticle distance is shorter than $3R_g$ for all systems

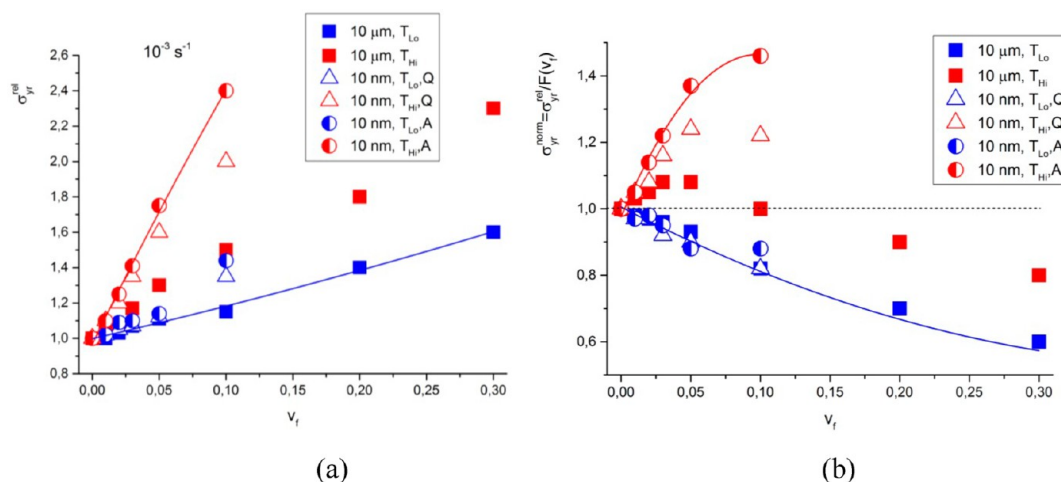


Figure 14. (a) Composition dependence of the rejuvenated yield stresses relative to that for neat PMMA, σ_{yr}^{rel} , measured at the strain rate of 10^{-3} s^{-1} at T_{Lo} (blue symbols) and T_{Hi} (red symbols) for microfilled (squares) and nanofilled PMMA (triangles-quenched, circles-annealed). (b) Composition dependence of the rejuvenated yield stress normalized to the volume replacement function (eq 4), $\sigma_{yr}^{norm} = [\sigma_{yr}^{rel}/F(\nu_f)]$ (symbols as in part a). The lines serve as the guide for the eyes.

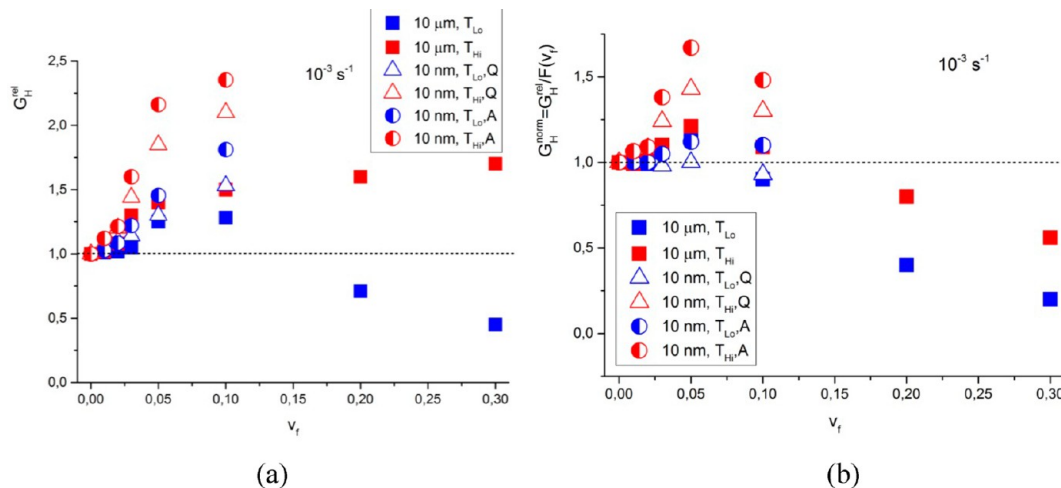


Figure 15. (a) Composition dependence of the strain hardening modulus relative to that for neat PMMA, $G_H^{rel} = G_H(\nu_f)/G_H(0)$, and (b) the G_H^{rel} normalized by the volume replacement function $F(\nu_f)$ (see eq 4, $G_H^{norm} = G_H^{rel}/\{1 + (2.5)\nu_f + P\nu_f^2\}$) measured at the strain rate of 10^{-3} s^{-1} at T_{Lo} and T_{Hi} for the micro- and nano-filled PMMA.

investigated.³⁶ Considering that $D \approx 10 \text{ nm}$ for the SiO_2 primary particles, and $R_g \approx 10 \text{ nm}$ for the PMMA used, $k \approx 1$. In the volume replacement models such as eq 4, the yield stress of the matrix, σ_{ym} , is assumed independent of the filler volume fraction. It has, however, been shown⁴⁹ that this assumption loses its validity for particles with diameter below 100 nm , at $\nu_f > 0.02$, and for T approaching T_g . The dependence of σ_{ym} on the filler content is attributed to the dramatic increase of the matrix-NP interface area upon adding large specific surface area NPs, making the fraction of chains with interface affected dynamics and packing substantial.

Figure 14b shows the corrections to the predictions of the volume-replacement model, i.e., $\sigma_{yr}^{rel}/F(\nu_f)$. These are also linear in ν_f , but (as expected) much larger and of opposite sign for T_{Hi} . In other words, at T_{Lo} , yield stress increases slightly ($\sim 10\%$) less than predicted by the volume-replacement model over the range of NP volume fractions considered here, while at T_{Hi} , it increases by about 30–40% more than predicted by this model. These opposing trends cannot be rationalized by inaccuracies in the functional form employed for $F(\nu_f)$. A more likely cause is that at

T_{Hi} , a significant fraction of chains (approaching 1 for $\nu_f = 0.05$) have interface retarded dynamics⁴⁶ that increase the flow stress relative to its value in neat PMMA.

We now turn to an analysis, in the same spirit, of the NP-loading dependence of strain hardening. $G_H^{rel} = G_H(\nu_f)/G_H(0)$ is shown in Figure 15a. The increase of G_H with NP loading is far more dramatic at T_{Hi} than at T_{Lo} , and also stronger for annealed samples than for quenched samples. The T dependence is consistent with the kinetic analyses of U_α discussed above; NPs increase the activation energy for strain hardening and hence the strain hardening modulus. Apparently the effect of thermal history persists throughout the strain hardening regime; this rather curious effect has been discussed above (Figure 7).

Comparison of the ν_f dependence of the G_H^{rel} to the predictions of the volume replacement function $F(\nu_f)$ (eq 4) also shows nontrivial effects, in particular a qualitatively different breakdown of the volume-replacement model. By assuming the same functional form for the ν_f dependence of G_H , eq 4 can be rearranged as

$$G_H^{norm} = \frac{G_H^{rel}}{(1 + (2.5k)v_f + Pv_f^2)}$$

where $F(v_f) = \{1 + (2.5)v_f + Pv_f^2\}$ is again given by a modified Einstein–Bachlor form. For hard spherical NPs that cannot transfer shear stress from the polymer matrix, G_H^{norm} should be v_f -independent; any deviation from this behavior from NPs altering chain packing and/or segmental dynamics. Values for G_H^{norm} with $k \approx 1$ and $P \approx 14$ are shown in Figure 15b. At T_{lo} , the volume replacement model predicts the v_f -dependence of G_H quite well, especially for quenched samples. The G_H^{norm} for the annealed samples exhibited small, approximately 10%, upward deviation from the simple volume replacement model above $v_f = 0.02$. In contrast, at T_{hi} the volume replacement model predicts only about 30% of the observed increase in G_H^{norm} with increasing v_f . Interestingly, in contrast to the deviation for $\sigma_{yr}^{rel}/F(v_f)$, the v_f -dependence is highly nonlinear.

Above $v_f = 0.03$ ($S_f = 28 \text{ m}^2/\text{cm}^3$), the average distance between 10 nm diameter primary SiO_2 nanoparticles (see Figure 6) becomes smaller than the R_g of the PMMA used. Thus, almost all of the chains are in contact with the NP surface and should exhibit some degree of retardation of their segmental dynamics and packing frustration. Hence, above $v_f = 0.03$, further addition of NPs did not increase the number of SiO_2 affected chains significantly. This resulted in a saturation. A similar effect was previously reported⁵⁰ for the saturation of the terminal relaxation time in PVAc/HAP nanocomposites.

We interpret these results as follows: at T_{lo} , the difference between interface and bulk chain dynamics is negligible and NP–NP pair interactions dominate. We propose that at T_{hi} the observed deviation must be related to reduced segmental mobility and modified segmental packing at the PMMA– SiO_2 interface. Frustration in chain packing has been proposed to play an important role in thermodynamic and dynamic properties of block copolymers as well as neat and NP-filled polymeric melts and glasses.^{29,51–53,64} For strong interfacial attraction, the packing becomes frustrated in the vicinity of the interface due to retarded segmental mobility, while for repulsive interfacial interaction, the frustrated region is shifted away from the interface due to the interface accelerated segmental mobility.^{54,55} At T_{hi} the volume-averaged terminal relaxation time should become strongly affected by the large volume of segments with PMMA– SiO_2 interface retarded dynamics and modified packing frustration, causing a strong deviation of the G_H^{norm} from the simple particle pair interaction dominating at T_{lo} . This suggests that G_H^{rel} can be expressed as a product of the strain hardening modulus for neat PMMA and some unknown function of (i) the specific interface area per cm^3 of the nanocomposite, S_f and (ii) the strength of the interfacial interactions.

Finally, we turn to the scaling of G_H with σ_{yr} (Figure 16). This scaling^{2–4,13} has its justification in the common origin of G_H and σ_{yr} in dissipative local segment-scale dynamical events.²⁰ Govaert et al.¹³ showed experimentally that linear relationships exist between G_H and σ_{flow} (measured from the minimum of the stress–strain curves) for a range of polymer glasses. However, these dependences exhibit chemistry-dependent (polymer specific) slopes. Here we take the alternate approach of examining the scaling for a single chemistry (PMMA) as a function of v_f and plot G_H against the “true” flow (i.e., rejuvenated yield) stress, σ_{yr} rather than against the “apparent” flow stress σ_{flow} obtained from the minima of stress–strain curves. Consistent with recent work, we find that G_H decreases

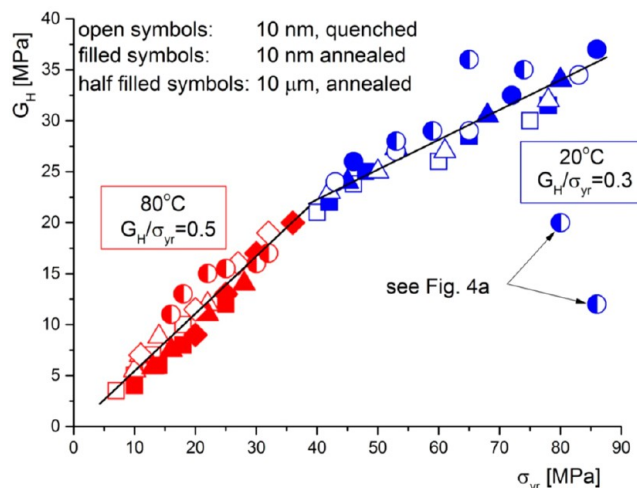


Figure 16. G_H scaling with the flow stress, σ_{yr} , for the microfilled PMMA and for the annealed neat and SiO_2 -filled PMMA. Red symbols represent T_{Hi} , blue symbols are for the T_{Lo} . Open symbols are for the quenched and solid symbols are for the annealed systems. Squares are for neat PMMA, circles for 1 vol % SiO_2 and triangles for 5 vol % SiO_2 . Data were fitted with two linear functions with slope $C_{Hi} = 0.50$ for low $\sigma_{yr} \leq 40$ MPa (high temperature) and $C_{Lo} = 0.3$ for $\sigma_{yr} \geq 40$ MPa (low temperature).

with increasing T , is strain rate dependent, and scales with the rejuvenated yield stress. This result is interesting in the sense that σ_{yr} and σ_{flow} are not equivalent. Linear G_H scaling with σ_{yr} is observed for both neat and SiO_2 -filled PMMA (Figure 16). The scaling law can be expressed in the simple form:

$$G_H(v_f) = G_{Hm} + C\sigma_{yr}(v_f)$$

The G_{Hm} is the intercept of the dependence expressed in eq 7 with the strain hardening modulus axis for $\sigma_{yr} = 0$. Our experimental data suggest that the G_{Hm} depends on the specific PMMA– SiO_2 interface area per cm^3 of the nanocomposite, S_f and temperature dependent PMMA– SiO_2 interfacial interaction energy, $\Delta E_{int}(T)$ (as in eq 5), similar to the intrinsic viscosity of a suspension of spherical particles:³²

$$G_{Hm} = G_{Hm}^0 \Phi(S_f, \Delta E_{int}) \quad (8)$$

In eq 8, the G_{Hm}^0 is the value of G_{Hm} for the neat PMMA ($v_f = 0$). It seems reasonable to assume that G_{Hm} will be a filler-chemistry controlled parameter.

Previous work^{20,47} showing rate-dependent, linear scaling of G_H with σ_{flow} has shown linear scaling, with a C that depends on testing conditions. However, it is interesting to attempt to collapse data for different test conditions onto a single master curve. Figure 16 summarizes all of our results for tests performed at different T (T_{hi} and T_{lo}), de/dt and v_f . The data here also show linear scaling with a T - and v_f -dependent slope, and the offset C increases with v_f . This shows that nanoparticles strengthen the coupling between plastic flow and strain hardening, presumably either by strengthening the coupling between molecular relaxation processes occurring on different length scales²⁴ or by nanoparticles acting as entanglement attractors which increase the rate of dissipative plastic events associated with strain hardening.¹¹ Analyzing this behavior using molecular simulations will be a focus of upcoming work. Finally, we note that system preparation protocol (quenched vs annealed) does not affect the scaling to within our experimental accuracy.

CONCLUSIONS

The fraction of chains affected by the presence of rigid, weakly attractively interacting nanoparticles is proportional to the specific interface area in per unit volume of the composite, S_f . As a result, no measurable effect of thermal history on large strain deformation behavior was observed in microcomposites. The use of S_f as the structural variable allows to separate the effect of the PMMA–particle interface area from the volume replacement contribution. Weakly attractive SiO₂–PMMA interactions increase the energy required to activate the segmental rearrangements associated with plastic flow in rejuvenated yielding and strain hardening. This justifies our use on NPs as “probes” of the local segmental dynamics and packing in PMMA. Moreover, our results confirm that the effect of rigid particles is more pronounced for the α process involving the entire backbone chain compared to the β process presumably involving only few segments. It also seems that the NPs slightly enhance the contribution of the β process to the overall value of G_H . This agrees with our hypothesis that the heterogeneous distribution of relaxation mechanisms in NP-filled PMMA is brought about by the differences in behavior between bulk and interface chains.

Rigid spherical nanoparticles increase the flow (rejuvenated yield) stress σ_{yr} and the strain hardening modulus, G_{Hh} in PMMA, with the extent of the enhancement being a function of T and NP loading. At $T_{lo} = T_g - 80$ K, the v_f dependence of G_H agrees reasonably well with predictions of a simple volume-replacement model. At $T_{hi} = T_g - 20$ K, strong divergence from the simple model was observed suggesting a substantial contribution of the volume of chains with interface retarded dynamics and modified packing frustration. G_H scales linearly with σ_{yr} , exhibiting two slopes equal to $C_{hi} = 0.50$ and $C_{lo} = 0.3$, respectively, at T_{hi} and T_{lo} . At T_{hi} , the $G_{Hm} = 0$ and, at T_{lo} , the G_{Hm} shifted to higher values proportionally to the specific PMMA–SiO₂ interface area, S_f . We speculate that the vertical shift of C_{lo} can be related (using e.g. the Adam–Gibbs theory⁵⁶) to the nanoparticle increasing the size of ensembles of cooperatively relaxing chain segments.

Our observations are consistent with our characterization of NP dispersion and extensive kinetic analyses. Good NP dispersion simplifies interpretation of our results in terms of segment-scale dynamics that are retarded by the attractive interactions between silica and PMMA. Kinetic analyses for both plastic flow and strain hardening show that activation energies uniformly increase with NP loading, while activation volumes exhibit complex behavior that depends on T , NP loading and strain. Finally, we have interpreted our results both in relation to the PNLE theory of Chen and Schweizer and in terms of how NPs and deformation alter systems' position on their energy landscapes. One key finding of our preparation-protocol-dependence studies is that the positions of quenched systems at T_{lo} and annealed systems at T_{hi} on their energy landscapes seem similar.

This collection of evidence clearly illustrates pronounced differences between thermally activated (melt-like) flow and stress-activated flow in glassy polymers. At low temperatures ($T_g - 80$ K), the polymer dynamics are affected by the nanoparticles during large active deformations in a similar fashion to that observed at much smaller deformations. As the temperature is increased ($T_g - 20$ K), the influence of the nanoparticles on the large-strain inelastic deformation is more pronounced and reminiscent of that observed in polymer melts and rubbers.

AUTHOR INFORMATION

Corresponding Author

*E-mail: (J.J.) josef.jancar@ceitec.vutbr.cz.

Notes

The authors declare no competing financial interest.

ACKNOWLEDGMENTS

Financial support under Project CZ.1.05/1.1.00/02.068 CEITEC from the EC and from the University of South Florida College of Arts and Sciences is greatly appreciated.

REFERENCES

- (1) Haward, R. N.; Young, R. J., Eds. *The Physics of Glassy Polymers*; Chapman and Hall: New York, 1997.
- (2) van Melick, H. G. H.; Govaert, L. E.; Meijer, H. E. H. *Polymer* **2003**, *44*, 2493.
- (3) Meijer, H. E. H.; Govaert, L. E. *Prog. Polym. Sci.* **2005**, *30*, 915.
- (4) Klompen, E. T. J.; Engels, T. A. P.; Govaert, L. E.; Meijer, H. E. H. *Macromolecules* **2005**, *38*, 6997.
- (5) Wendlandt, M.; Tervoort, T. A.; Suter, U. W. *Polymer* **2005**, *46*, 11786.
- (6) van Breemen, L. C. A.; Engels, T. A. P.; Klompen, E. T. J.; Senden, D. J. A.; Govaert, L. E. *J. Polym. Sci., Part B: Polym. Phys.* **2012**, *50*, 1757.
- (7) Senden, D. J. A.; Krop, S.; van Dommelen, J. A. W.; Govaert, L. E. *J. Polym. Sci., Part B: Polym. Phys.* **2012**, *50*, 1680.
- (8) Fielding, S. M.; Larson, R. G.; Cates, M. E. *Phys. Rev. Lett.* **2012**, *108*, 048301.
- (9) Chen, K.; Saltzman, E. J.; Schweizer, K. S. *Annu. Rev. Condens. Matter Phys.* **2010**, *1*, 277.
- (10) Hoy, R. S.; Robbins, M. O. *J. Polym. Sci., Part B: Polym. Phys.* **2006**, *44*, 3487–3500.
- (11) Hoy, R. S.; Robbins, M. O. *Phys. Rev. E* **2008**, *77*, 031801.
- (12) Hoy, R. S.; Robbins, M. O. *J. Chem. Phys.* **2009**, *130*, 244901.
- (13) Govaert, L. E.; Engels, T. A. P.; Wendlandt, M.; Tervoort, T. A.; Suter, U. W. *J. Polym. Sci., Part B: Polym. Phys.* **2008**, *46*, 2475.
- (14) Loo, L. S.; Cohen, R. E.; Gleason, K. K. *Science* **2000**, *288*, 116.
- (15) Capaldi, F. M.; Boyce, M. C.; Rutledge, G. C. *Phys. Rev. Lett.* **2002**, *89*, 175505.
- (16) Chen, K.; Schweizer, K. S. *Macromolecules* **2008**, *41*, 5908.
- (17) Chen, K.; Schweizer, K. S. *Phys. Rev. Lett.* **2009**, *102*, 038301.
- (18) Chen, K.; Schweizer, K. S. *Phys. Rev. E* **2010**, *82*, 041804.
- (19) Chen, K.; Schweizer, K. S. *Macromolecules* **2011**, *44*, 3988–4000.
- (20) Lee, H. N.; Riggleman, R. A.; de Pablo, J. J.; Ediger, M. D. *Macromolecules* **2009**, *42*, 4328.
- (21) Lee, H. N.; Paeng, K.; Swallen, S. F.; Ediger, M. D. *Science* **2009**, *323*, 231.
- (22) Riggleman, R. A.; Lee, H.-N.; Ediger, M. D.; de Pablo, J.-J. *Soft Matter* **2010**, *6*, 287.
- (23) Stachurski, Z. H. *Polymer* **2003**, *44*, 6067.
- (24) Hoy, R. S. *J. Polym. Sci., Part B: Polym. Phys.* **2011**, *49*, 979.
- (25) Lyulin, A. V.; Hudzinskyy, D.; Janiaud, E.; Chateuminois, A. J. *Non-Cryst. Solids* **2011**, *357*, 567–574.
- (26) Kramer, E. J. *Adv. Polym. Sci.* **1983**, *52–53*, 1.
- (27) Jancar, J.; Douglas, J. F.; Starr, F. W.; Kumar, S. K.; Cassagnau, P.; Lesser, A. J.; Sternstein, S. S.; Buehler, M. J. *Polymer* **2010**, *51*, 3321.
- (28) Akcora, P.; Liu, H.; Kumar, S. K.; Moll, J.; Li, Y.; Benicewicz, B. C.; Schadler, L. S.; Acehin, D.; Panagiotopoulos, A. Z.; Pryamitsyn, V.; Ganesan, V.; Ilavsky, J.; Thiyagarajan, P.; Colby, R. H.; Douglas, J. F. *Nat. Mater.* **2009**, *8*, 354.
- (29) Akcora, P.; Kumar, S. K.; Moll, J.; Lewis, S.; Schadler, L. S.; Li, Y.; Benicewicz, B. C.; Sandy, A.; Narayanan, S.; Ilavsky, J.; Thiyagarajan, P.; Colby, R. H.; Douglas, J. F. *Macromolecules* **2010**, *43*, 1003.
- (30) Robbins, M. O.; Hoy, R. S. *J. Polym. Sci., Part B: Polym. Phys.* **2009**, *47*, 1406.
- (31) Hoy, R. S.; O'Hern, C. S. *Phys. Rev. E* **2010**, *82*, 041803.
- (32) Riggleman, R. A.; Toepperwein, G.; Papakonstantopoulos, G. J.; Barrat, J.-L.; De Pablo, J. J. *J. Chem. Phys.* **2009**, *130*, 244903.

- (33) Castrillo, P. D.; Olmos, D.; Amador, D. R.; Gonz ales-Benito, J. J. *Colloid Interface Sci.* **2007**, *308*, 318.
- (34) Goren, K.; Okan, O. B.; Chen, L.; Schadler, L. S.; Ozisik, R. J. *Supercrit. Fluids* **2012**, *67*, 108.
- (35) Arce, V. B.; Bertolotti, S. G.; Oliveira, J. V. E.; Airolidi, C.; Gonz ales, M. C.; Alegretti, P. E.; M artire, D. O. *Spectrochim. Acta, Part A: Mol. Biomol. Spectrosc.* **2009**, *73*, 54.
- (36) Anderson, B. J.; Zukoski, C. F. *Macromolecules* **2009**, *42*, 8370.
- (37) Kabanemi, K. K.; H etu, J.-F. *J Non-Newtonian Fluid Mech.* **2010**, *165*, 866.
- (38) Zidek, J.; Kucera, J.; Jancar, J. *Comput., Mater. Continua* **2010**, *16*, 51.
- (39) Starr, F. S.; Douglas, J. F. *Phys. Rev. Lett.* **2011**, *106*, 115702.
- (40) Allegra, G.; Raos, G.; Vacatello, M. *Prog. Polym. Sci.* **2008**, *33*, 683–731.
- (41) Parker, K.; Schneider, R. T.; Siegel, R. W.; Ozisik, R.; Cabanelas, J. C.; Serrano, B.; Antonelli, C.; Baselga, J. *Polymer* **2010**, *51*, 4891.
- (42) Ash, B. J.; Schadler, L. S.; Siegel, R. W. *Mater. Lett.* **2002**, *55*, 83.
- (43) Littunen, K.; Hippi, U.; Saarinen, T.; Sepp al , J. *Carbohydr. Polym.* **2013**, *91*, 183.
- (44) Ahmad, S.; Bohidar, H. B.; Ahmad, S.; Agnihotry, S. A. *Polymer* **2006**, *47*, 3583.
- (45) D zunozovi , E.; Jaremi , K.; Nedeljkovi , J. M. *Eur. Polym. J.* **2007**, *43*, 3719.
- (46) Sastry, S.; Debenedetti, P. G.; Stillinger, F. H. *Nature* **1998**, *393*, 554.
- (47) Roetling, J. A. *Polymer* **1965**, *6*, 311.
- (48) Eyring, H. J. *J. Chem. Phys.* **1936**, *4*, 283.
- (49) Jancar, J.; Recman, L. *Polymer* **2010**, *51*, 3826.
- (50) Kalfus, J.; Jancar, J. *J. Polym. Sci., B: Polym. Phys.* **2007**, *45*, 1380.
- (51) Riggleman, R. A.; Douglas, J. F.; de Pablo, J. J. *J. Chem. Phys.* **2007**, *126*, 234903.
- (52) Grason, G. M. *Phys. Rep.* **2006**, *433*, 1.
- (53) Wong, H.C.; Sanz, A.; Douglas, J. F.; Cabral, J. T. *J. Mol. Liquids* **2010**, *153*, 79.
- (54) Knorowski, C. D.; Anderson, J. A.; Travesset, A. *J. Chem. Phys.* **2008**, *128*, 164903.
- (55) Kumar, J.; Goswami, M.; Sumpter, B. G.; Novikov, V. N.; Sokolov, A. P. *Phys. Chem. Chem. Phys.* **2013**, *15*, 4604.
- (56) Starr, F. S.; Douglas, J. F. *Phys. Rev. Lett.* **2011**, *106*, 115702.
- (57) Li, C.; Wu, J.; Zhao, J.; Zhao, D.; Fan, Q. *Eur. Polym. J.* **2004**, *40*, 1807.
- (58) Doxastakis, M.; Chen, Y.-L.; Guzm n, O.; de Pablo, J. J. *J. Chem. Phys.* **2004**, *120*, 9335–9342.
- (59) Papakonstantopoulos, G. J.; Yoshimoto, K.; Doxastakis, M.; Nealey, P. F.; de Pablo, J. J. *Phys Rev E* **2005**, *72*, 031801.
- (60) Rottler, J.; Robbins, M. O. *Phys. Rev. E.* **2003**, *68*, 011507.
- (61) Ree, T.; Eyring, H. *J. Appl. Phys.* **1955**, *26*, 793.
- (62) van Breemen, L. C. A.; Engels, T. A. P.; Klompen, E. T. J. J. A.; Senden, D. J. A.; Govaert, L. E. *J. Polym. Sci., Polym. Phys.* **2012**, *50*, 1757.
- (63) Bergman, R.; Alvarez, F.; Alegr a, A.; Colmenero, J. *J. Non-Cryst. Solids* **1998**, *235–237*, 580.
- (64) Perez, J.; Caville, J. Y.; David, L. *J. Mol. Struct.* **1999**, *479*, 103.
- (65) Klompten, E. T. *J. Mechanical Properties of Solid Polymers*. Ph.D. Thesis, TU Eindhoven, 2005
- (66) Kobayashi, H.; Takayashi, H.; Hiki, Y. *J. Non-Cryst. Solids* **2001**, *290*, 32.
- (67) Kalfus, J.; Jancar, J. *Polymer* **2007**, *48*, 3935.
- (68) $V_\alpha V_\beta \Delta U_\alpha \Delta U_\beta$, $d\epsilon_{0,\alpha}/dt$ and $d\epsilon_{0,\beta}/dt$ for the yield stress have been determined by fitting equations similar to eq 2 with experimental σ_y/T vs $\log(d\epsilon/dt)$ data^{47,62,66} or from dielectric^{57,63} and dynamic mechanical spectroscopy.⁶⁷ Published values of ΔU_α range widely from⁵⁷ 150 kJmol⁻¹ to⁶⁷ 668 kJmol⁻¹, while most of the published values of ΔU_β range between⁶³ 80 and⁴⁷ 100 kJ mol⁻¹. Similarly, values of the rate constant $d\epsilon_{0,\alpha}/dt$ vary from⁶² $6 \times 10^{25} \text{ s}^{-1}$ to⁶⁶ $6 \times 10^{35} \text{ s}^{-1}$ while the published $d\epsilon_{0,\beta}/dt$ varies between⁶⁶ $3.2 \times 10^{11} \text{ s}^{-1}$ and⁶² $3.3 \times 10^{13} \text{ s}^{-1}$.